JGR Solid Earth

RESEARCH ARTICLE
10.1029/2018JB017171

# Mountain Building or Backarc Extension in Ocean-Continent Subduction Systems: A Function of Backarc Lithospheric Strength and Absolute Plate Velocities

**Sebastian G. Wolf**[1] **and Ritske S. Huismans**[1]

[1]Department of Earth Science, University of Bergen, Bergen, Norway

**Key Points:**
- Weak and removed backarc lithospheric mantle facilitates overriding plate deformation
- Trench-ward overriding plate movement inhibits backarc extension and is necessary for backarc shortening
- Comparison with the central Andean and Hellenic subduction zones corroborates model inferences

**Supporting Information:**
- Supporting Information S1
- Movie S1
- Movie S2
- Movie S3
- Movie S4
- Movie S5
- Movie S6
- Movie S7
- Movie S8
- Movie S9
- Movie S10
- Movie S11
- Movie S12

**Correspondence to:**
S. G. Wolf,
sebastian.wolf@uib.no

**Citation:**
Wolf, S. G., & Huismans, R. S. (2019). Mountain building or backarc extension in ocean-continent subduction systems: A function of backarc lithospheric strength and absolute plate velocities. *Journal of Geophysical Research: Solid Earth*, *124*, 7461–7482. https://doi.org/10.1029/2018JB017171

Received 12 DEC 2018
Accepted 22 MAY 2019
Accepted article online 31 MAY 2019
Published online 29 JUL 2019



**Abstract** The crustal structure of overriding plates in subduction settings around the world varies between a wide range of deformation styles, ranging from extensional structures and backarc opening as in the Tonga or Hellenic subduction zone to large, plateau-like orogens such as the central Andes. Both end-member types have been intensively studied over the last decades, and several hypotheses have been proposed to explain their characteristics. Here we model ocean-continent collision using high-resolution, upper mantle scale plane-strain thermo-mechanical models, accounting for phase changes of rocks that enter the eclogite stability field and the phase transition at the 660 km mantle discontinuity. We test model sensitivity to varying plate velocities and backarc lithospheric strength as the main variables affecting the strain regime of the overriding plate in subduction zones. With our small set of variables, we reproduce both overriding plate extension and shortening and provide insight into the dynamics behind those processes. We find that absolute plate velocities determine the possible strain regimes in the overriding plate, where overriding plate movement toward the trench inhibits backarc extension and promotes overriding plate shortening. Additionally, a weak and removed backarc lithospheric mantle is required for backarc extension and facilitates overriding plate shortening. Comparison of the models with natural subduction systems, specifically the Andes and Hellenic subduction zones, corroborates that lithospheric removal and absolute plate velocities guide overriding plate deformation.

## 1. Introduction

The overriding plate in ocean-continent subduction systems on Earth has variable tectonic styles. Typical end-members (Uyeda & Kanamori, 1979) are backarc extension as in the Marianas or Hellenic subduction zone (Faccenna et al., 2014; Jolivet et al., 2013) and large orogenic plateau formation as in the central Andes with up to several hundreds of kilometers of overriding plate shortening (Arriagada et al., 2008; Oncken et al., 2006). During recent years, a multitude of geodynamic models (e.g., Agrusta et al., 2017; Arcay et al., 2006; Becker et al., 1999; Billen, 2008, 2010; Butler & Beaumont, 2017; Capitanio et al., 2007, 2010; Cizkova et al., 2002; Currie et al., 2008; Duretz et al., 2012; Faccenda et al., 2012, Faccenna et al., 2017; Funiciello et al., 2003, 2004; Gerya, 2011, Gerya et al., 2015; Holt et al., 2015; Morra et al., 2006; Schellart et al., 2007; Schmeling et al., 2008; Sobolev & Babeyko, 2005; Quinquis et al., 2011) highlights different aspects of subduction dynamics, but no set of working geodynamical models provides and summarizes the main factors which induce either overriding plate extension or shortening in ocean-continent subduction systems.

The tectonic plates on Earth move with absolute velocities of 0 to 10 cm/yr. Those that have a subducting oceanic slab attached to one of their boundaries move in the subduction direction and are significantly faster (3–10 cm/yr) than plates without an attached slab (0–3 cm/yr; Kreemer et al., 2003; O'Neill et al., 2005; Schellart et al., 2007, 2008). This indicates that slab pull, the negative buoyancy of the downgoing slab, provides a first-order control on plate movement (Forsyth & Uyeda, 1975). Slab pull is counteracted by shearing at the subduction interface, rheology-dependent slab deformation, slab suction, and P-T-dependent phase changes in the transition zone (Agrusta et al., 2017; Billen, 2008; Funiciello et al., 2003; Rodriguez-Gonzalez & Negredo, 2012; Sobolev & Babeyko, 2005). The combination of these factors leads to a "natural" sinking velocity ($v_{sink}$) of slabs in the mantle (Faccenna et al., 2014). In an isolated system, $v_{sink}$ is accommodated by

the combined convergence rates of the subducting plate ($v_{oc}$) and the overriding plate ($v_{cont}$), and deformation occurs mostly at the subduction interface and not inside the plates (Capitanio et al., 2010). However, tectonic plates are no isolated features, have lateral density and viscosity variations, possibly several subducting edges (e.g., Pacific plate), and are dragged or pushed by topographic differences (e.g., ridge push) or sublithospheric mantle flow. These factors modify plate velocities and generate tensional or compressional tectonic stresses which can induce extension or shortening in the overriding plate.

The question why the overriding plate in subduction systems deforms has been addressed by several global statistical analyses (Heuret & Lallemand, 2005; Jarrard, 1986; Schellart, 2008), suggesting that overriding plate movement toward or away from the subduction zone provides a main control for variable overriding plate deformation, as already proposed by Uyeda and Kanamori (1979). Numerical modeling confirms that overriding plate movement toward the trench is crucial for mountain building (Sobolev & Babeyko, 2005), while a stationary plate with weak lithosphere promotes backarc spreading (Capitanio et al., 2010). Additionally, the efficiency of toroidal return flow around slab edges is shown to provide an important constraint on the propensity for slab retreat or advance (Funiciello et al., 2004; Schellart & Moresi, 2013; Schellart et al., 2007). Furthermore, large-scale poloidal mantle flow and local subduction-related upwellings have been suggested as a driving force for overriding plate deformation (Faccenna et al., 2010, 2017; Holt et al., 2015; Husson et al., 2012).

Seismological studies show that subduction zones exhibit not only contrasting overriding plate strain regimes but also variable structure at depth (Goes et al., 2017; Li et al., 2008). The two end-member styles are slabs that flatten out in the lower mantle transition zone (e.g., Japan-Izu-Bonin) and those that pierce directly into the lower mantle (e.g., Marianas). Slab stagnation for subduction zones with significant trench retreat has been attributed to the combined effects of the viscosity increase and positive buoyancy associated with the negative Clapeyron slope of the ringwoodite to bridgemanite and magnesiowüstite transition (Agrusta et al., 2017; Billen, 2010; Goes et al., 2017).

Although differing in overriding plate strain regime and deep structural style, many subduction zone backarcs are characterized by elevated heat flow values (Hyndman et al., 2005). While this is expected for regions with active backarc spreading, it requires an explanation for areas with an intact overriding plate. Currie et al. (2008) show with thermo-mechanical modeling that the high heat flow values may result from convective removal of the backarc lithospheric mantle. This requires a weakened backarc lithospheric mantle, for instances, related to fluids expelled from the subducting slab, inherited from earlier deformation periods or subduction-associated melting (Arcay et al., 2005, 2006; Faccenda et al., 2012). Removal of the backarc lithospheric mantle may be enhanced by foundering of dense melt residues (Currie et al., 2015; DeCelles et al., 2009).

We integrate these observations in a geodynamic model and investigate the influence of variable plate velocities and backarc lithospheric strength on the overriding plate strain regime. To advance our understanding of the controlling factors, we use whole mantle scale 2-D thermo-mechanically coupled numerical models that account for the phase transition at the 660 km mantle discontinuity. Our goal is to identify the main factors that control overriding plate extension or shortening and to extract characteristic tectonic and evolutionary features from our models.

Next we present the governing equations and setup of our modeling approach, followed by the model results and an analysis of driving and resisting forces. We then discuss the main parameters leading to overriding plate extension or shortening and compare our model inferences with the central Andes and the Hellenic subduction zone.

## 2. Methodology

### 2.1. Basic Principles

We use a modified version of the two-dimensional Arbitrary Lagrangian-Eulerian, thermo-mechanically coupled finite element code FANTOM (Erdos et al., 2014; Thieulot, 2011) to model ocean-continent subduction. We solve for plane-strain incompressible creeping (Stokes) flows ((1) and (2)) and heat transfer (3) in the model domain:

$$\frac{\partial v_i}{\partial x_i} = 0 \quad i = 1, 2, \tag{1}$$

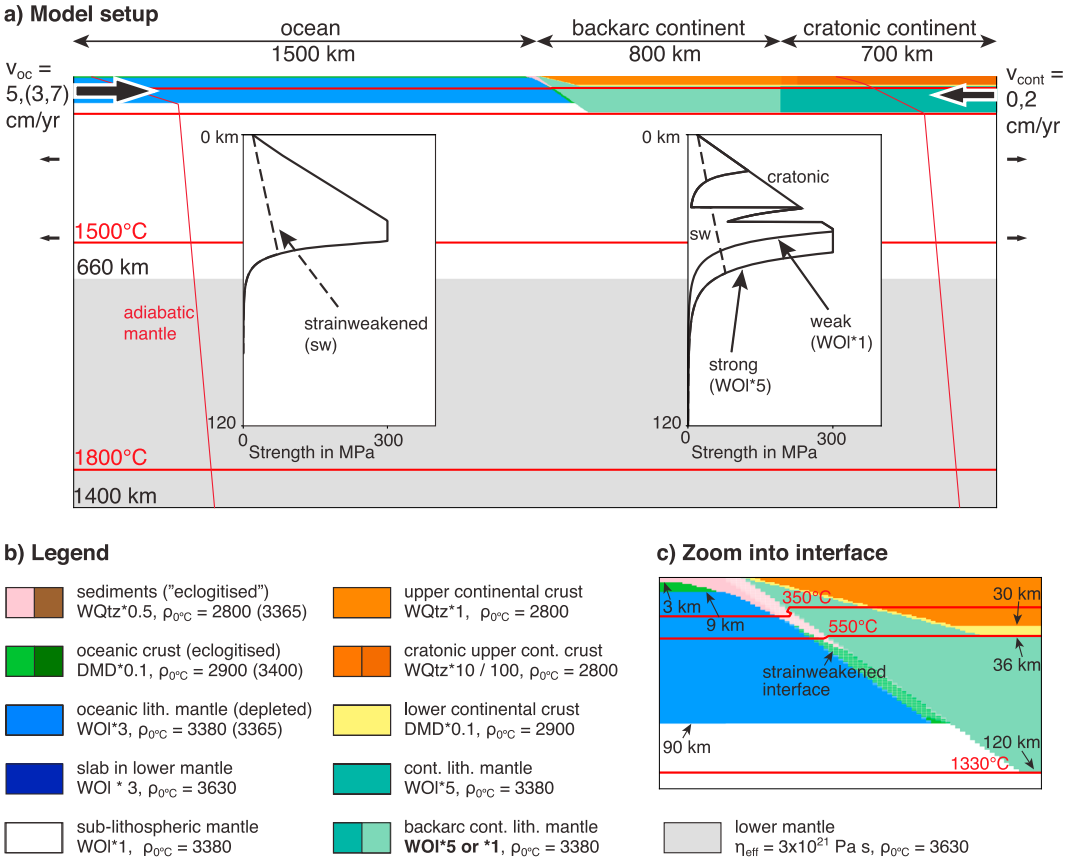


**Figure 1.** Initial model setup and boundary conditions. (a) The model consists of an oceanic and a continental domain overlying a sublithospheric upper and lower mantle. During model run, we apply a constant velocity boundary condition $v_{oc} = 3$, 5, and 7 cm/yr and $v_{cont} = 0$ and 2 cm/yr in, respectively, the oceanic and continental lithospheres. Inflow of oceanic material is balanced by outflow of the same amount of material on both sides of the sublithospheric upper mantle, and inflow of continental material is compensated by outflow of sublithospheric upper mantle on the continental side. The upper surface is free, and the side and bottom boundaries have free slip boundary conditions. The initial temperature profile of the continent corresponds to 1-D thermal steady state, and the underlying mantle has an adiabatic gradient of 0.4 °C/km. The side boundaries are insulated, and the bottom boundary has a fixed temperature boundary condition of 1,850 °C. The temperature in the oceanic lithosphere is linearly increasing from 0 to 1,314 °C resulting in a uniform temperature distribution. The inserts show initial yield strength envelopes of the oceanic and continental model domains. (b) Legend with scaled flow law and density in kilograms per cubic meter. WQtz is the wet quartz flow law as described in Gleason and Tullis (1995), DMD is the dry Maryland flow law from Mackwell et al. (1998), and WOl is the wet olivine flow law from Karato and Wu (1993). (c) Zoom into the interface between the two plates. The white overlay at the interface masks the initially strain-weakened region.

$$\frac{\partial \sigma_{ij}}{\partial x_i} + \rho g = 0 \quad i, j = 1, 2, \tag{2}$$

$$c_p \rho \left( \frac{\partial T}{\partial t} + v_i \frac{\partial T}{\partial x_i} \right) = k \frac{\partial}{\partial x_i} \frac{\partial T}{\partial x_i} + H + v_j \alpha \rho T g, \tag{3}$$

where $v_i$ are velocity components, $x_i$ are spatial coordinates, $\sigma_{ij}$ is the stress tensor, $\rho$ is density, $g$ is gravitational acceleration, $c_p$ is specific heat, $T$ is temperature, $t$ is time, $k$ is thermal conductivity, $H$ is radioactive heat production per unit volume, and $\alpha$ is the volumetric thermal expansion coefficient. The last term in (3) is the correction for adiabatic heating when material moves vertically.

For viscous deformation, a nonlinear, thermally activated power law creep formulation is used which relates pressure, temperature, and strain rate to the effective viscous flow stress, $\sigma'_{visc}$:

$$\sigma'_{visc} = f \cdot A^{-\frac{1}{n}} \cdot (\dot{\epsilon}_{eff})^{\frac{1}{n}} \cdot exp\left( \frac{Q + VP}{nRT} \right), \tag{4}$$

where $\sigma'_{visc}$ is the square root of the second invariant of the deviatoric stress, $\dot{\epsilon}_{eff}$ is the square root of the second invariant of the deviatoric strain rate, $f$ is a scaling factor, $A$ the preexponential factor converted to plane strain, $n$ the power law exponent, $Q$ activation energy, $V$ activation volume, $P$ the dynamic pressure, and $R$ the universal gas constant. We base our model materials on well-established flow laws and use the scaling factor $f$ to account for uncertainties resulting from extrapolation from laboratory to natural conditions and different geological settings: wet quartz (Gleason & Tullis, 1995), dry Maryland diabase (Mackwell et al., 1998), and wet olivine (Karato & Wu, 1993).

Frictional-plastic deformation of the materials is approximated using a pressure-dependent Drucker-Prager yield criterion:

$$\sigma'_{plast} = P \cdot \sin(\phi_{eff}) + C \cdot \cos(\phi_{eff}), \tag{5}$$

where $\sigma'_{plast}$ is the square root of the second invariant of the deviatoric stress, $P$ is the dynamic pressure, $\phi_{eff}$ is the effective angle of internal friction, and $C$ is cohesion. Strain weakening is accounted for by linearly reducing $\phi_{eff}$ from 15° to 2° through a predefined strain ($\epsilon$) interval $0.4 < \epsilon < 1.4$ (Huismans & Beaumont, 2003).

The main deformation mechanism for olivine at high pressures, high differential stresses, and low temperatures is a temperature-insensitive exponential creep (Katayama & Karato, 2008; Tsenn & Carter, 1987). We approximate this deformation mechanism by limiting the plastic yield stress of all model materials based on the wet olivine flaw to $\sigma'_{plast} \leq 300$ MPa (e.g., Andrews & Billen, 2009; Butler et al., 2015).

The density of the model materials is temperature dependent and given by $\rho(T) = \rho_0 \cdot (1 - \alpha(T - T_0))$. The T-P dependence of $\alpha$ in olivine and its polymorphs (Tosi et al., 2013) is approximated by linearly increasing $\alpha$ from $3 \times 10^{-5}$ to $4 \times 10^{-5}$ $K^{-1}$ in the temperature range of 500–2,000 K (e.g., Butler et al., 2015) and linearly decreasing $\alpha$ by a factor 1 to 0.5 between 0 to 45 GPa (Agrusta et al., 2017; Tosi et al., 2013).

### 2.2. Model Setup

Oceanic subduction under continental lithosphere is modeled using an idealized mantle scale model domain with 3,000 km horizontal and 1,400 km vertical extent (Figure 1 and Table 1). The oceanic lithosphere is composed of 3 km sediments, 6 km oceanic crust, and a 81 km thick lithospheric mantle which is depleted by 15 kg/m$^3$ down to a depth of 70 km. The continental domain, subdivided into backarc and cratonic continent, is composed of 30 km upper and middle crust and 6 km lower crust (Hacker et al., 2011; Huang et al., 2013; see also supporting information S1), underlain by lithospheric mantle up to a depth of 120 km. The width of the backarc domain in the overriding plate follows Currie et al. (2008). Tests with smaller or wider backarc domains gave similar results. The sublithosperic upper mantle ranges to 660 km depth with lower mantle between 660 km depth and the lower model boundary at 1,400 km. All materials have the same plastic parameters apart from oceanic sediments, which are additionally affected by strain weakening of the cohesion to focus deformation into the sediments that enter the subduction channel. The choice of modeling parameters follows earlier similar studies (Butler et al., 2015; Currie et al., 2008; Huismans & Beaumont, 2011; Pysklywec & Beaumont, 2004).

Viscous flow of the continental upper and middle crust follows a wet Quartz flow law (Gleason & Tullis, 1995). Cratonic crust is scaled by a factor of 10 and 100, accounting for stronger upper crust coupled to the mantle lithosphere. The oceanic and lower continental crust follow a dry Maryland diabase flow law (Mackwell et al., 1998) scaled by a factor $f = 0.1$, representing partially hydrated strong mafic crust. Oceanic and continental lithospheric mantle rheologies are based on wet olivine (Karato & Wu, 1993), respectively, scaled by $f = 3$ and $f = 5$, representing dry, depleted lithospheric mantle. Models with a "weak" backarc have a backarc lithospheric mantle with the same rheology and compositional density as the underlying mantle. The sublithospheric mantle follows a wet olivine flow law with $f = 1$, resulting in a viscosity profile consistent with Mitrovica and Forte (2004). Lower mantle rheology is subject to a large range of uncertainties with viscosity estimated between $1 \times 10^{21}$ and $5 \times 10^{22}$ Pa s (Billen, 2010; Mitrovica & Forte, 2004). We adopt a uniform viscosity of $3 \times 10^{21}$ Pa s for the lower mantle, leading to a viscosity increase at the 660 km discontinuity of approximately a factor of 30. All material that sinks below 1,200 km depth is converted to lower mantle to prevent interaction of the slab with the lower model boundary.

The initial temperature distribution reflects average values in the continental domain (Hacker et al., 2015), with a Moho temperature of ~550 °C and a 120 km thick lithosphere with 1,330 °C at its base, resulting in

Journal of Geophysical Research: Solid Earth

10.1029/2018JB017171

**Table 1**
*Mechanical and Thermal Properties of the Materials*

| | Oceanic plate | | | Continental plate | | | | |
|---|---|---|---|---|---|---|---|---|
| Parameters | Sediments | Crust | Mantle lithosphere | Upper/middle crust (cratonic) | Lower crust | Mantle lithosphere (**weak**) | Sublithospheric mantle | Lower mantle |
| *Plastic rheology* | | | | | | | | |
| C - $C_{sw}$ (MPa) | 20–4 | 20–20 | 20–20 | 20–20 | 20–20 | 20–20 | 20–20 | — |
| $\phi - \phi_{sw}$ (°) | 15–2 | 15–2 | 15–2 | 15–2 | 15–2 | 15–2 | 15–2 | — |
| *Viscous rheology* | | | | | | | | |
| Flow law | WQtz | DMD | WOl | WQtz | DMD | WOl | WOl | constant |
| f | 0.5 | 0.1 | 3 | 1 (10;100) | 0.1 | 5 (**1**) | 1 | viscosity of |
| A (Pa $s^{1/n}$)[a] | $8.57 \times 10^{-28}$ | $5.78 \times 10^{-27}$ | $1.76 \times 10^{-14}$ | $8.57 \times 10^{-28}$ | $5.78 \times 10^{-27}$ | $1.76 \times 10^{-14}$ | $1.76 \times 10^{-14}$ | $3 \times 10^{21}$ Pa s |
| n | 4.0 | 4.7 | 3.0 | 4.0 | 4.7 | 3.0 | 3.0 | — |
| Q (kJ/mol) | 223 | 485 | 430 | 223 | 485 | 430 | 430 | — |
| V ($cm^3$/mol) | 0 | 0 | $1.1 \times 10^{-5}$ | 0 | 0 | $1.1 \times 10^{-5}$ | $1.1 \times 10^{-5}$ | — |
| *Density parameters* | | | | | | | | |
| $\rho_0$ (kg/$m^3$) | 2,800 (3,365)[b] | 2,900 (3,400)[b] | 3,380/3,365 (depleted) | 2,800 | 3,000 | 3,380 | 3,380 | 3,630 |
| $\alpha$ ($K^{-1}$)[c] | $3 \times 10^{-5}$ | $3 \times 10^{-5}$ | $2 \times 10^{-5}$–$4 \times 10^{-5}$ | $3 \times 10^{-5}$ | $3 \times 10^{-5}$ | $2 \times 10^{-5}$–$4 \times 10^{-5}$ | $2 \times 10^{-5}$–$4 \times 10^{-5}$ | $2 \times 10^{-5}$–$4 \times 10^{-5}$ |
| *Thermal parameters* | | | | | | | | |
| k ($Wm^{-1}K^{-1}$) | 2.25 | 2.25 | 2.25 | 2.25 | 2.25 | 2.25 | 2.25[d] | 2.25[d] |
| H ($\mu W/m^3$) | 1.1 (0)[b] | 0 | 0 | 1.1 | 0.5 | 0 | 0 | 0 |
| $c_p$ (J $kg^{-1}$ K) | 750 | 750 | 1,250 | 750 | 750 | 1,250 | 1,250 | 1,250 |

*Note.* WQtz is the wet quartz flow law as described in Gleason and Tullis (1995); DMD is the dry Maryland flow law from Mackwell et al. (1998); and WOl is the wet olivine flow law from Karato and Wu (1993).
[a]The laboratory-derived preexponential flow law exponent has been converted to conform with the second invariants of the stress and strain rates used in the model approach. [b]Metamorphic high pressure equivalent. The P-T field for the metamorphic reaction coincides with the eclogite stability field from Hacker (1996). [c]For mantle materials, thermal expansion coefficient is P-T dependent with a linear increase from $3 \times 10^{-5}$ to $4 \times 10^{-5}$ $K^{-1}$ in the temperature range of 500–2,000 K and a linear decrease by a factor 1 to 0.5 from 0 to 45 GPa. [d]Thermal conductivity for low temperatures. Between 1,335 and 1,345 °C, the conductivity linearly increases from 2.25 to 52.0 W $m^{-1}$ $K^{-1}$; to mimic active mantle convection at high Nusselt number, keep the adiabatic gradient and prevent the system from cooling.

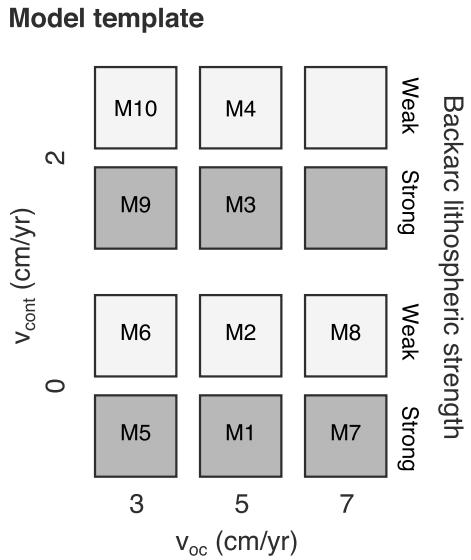


**Figure 2.** Template of models presented. Tested are the absolute subduction velocity ($v_{oc}$) and the overriding plate velocity ($v_{cont}$) with both a strong and weak backarc lithospheric mantle. M1 to M10 are the model numbers as used in the text.

a surface heat flow of 53 mW/m$^2$ and heat flux in the sublithospheric mantle of ~20 mW/m$^2$. We assume a 90 km thick oceanic lithosphere with a geotherm that increases linearly from 0 to 1,314 °C. This results in a uniform temperature distribution in the sublithospheric and lower mantle with an adiabatic gradient of 0.4 °C/km. The side boundaries are insulated, and the bottom boundary has a constant temperature of 1,850 °C.

To maintain the heat flux at the lithosphere-asthenosphere boundary and an adiabatic gradient of 0.4 °C/km in the sublithospheric upper and lower mantle, $k$ linearly increases from 2.25 to 52.0 W m$^{-1}$ K$^{-1}$ between 1,335 and 1,345 °C in the sublithospheric upper and lower mantle (Pysklywec & Beaumont, 2004). All other materials have a thermal conductivity $k$ = 2.25 W m$^{-1}$ K$^{-1}$.

The models include an irreversible metamorphic phase change of oceanic crust to eclogite when entering the stability field of eclogite (Hacker, 1996). Eclogite has the same viscous flow law as the oceanic crust but a different density. In order to keep the models simple, we assume that sediments obtain a higher, metamorphic density when entering the eclogite stability field. We acknowledge, however, that subduction of buoyant sediments can have strong implications for subduction dynamics (Currie et al., 2007; Hacker et al., 2015). All slab and mantle materials are subject to a reversible phase change with a Clapeyron slope of −2 MPa/K at the 660 km discontinuity, corresponding to the break down of ringwoodite to bridgemanite and magnesiowüstite (see discussion in Billen, 2010; Goes et al., 2017). For simplicity, slab materials are converted to one lower mantle material, which has the viscous flow law of the oceanic lithosphere. The phase changes do not account for latent heat and are not mass conserving. However, they illustrate the first-order effects of important metamorphic phase changes affecting subduction systems and are thus assumed to be sufficient.

Subduction is modeled using velocity boundary conditions on the sides of the model. Inflow of oceanic material is balanced by a small distributed outflow at both sides of the model in the sublithospheric upper mantle. Inflow of continental material is balanced by outflow only on the right, continental side (see Figure 1). Further boundary conditions are free slip at the model walls and base and a stress-free upper surface.

The Eulerian grid consists of 1,000 cells in the horizontal direction and 280 cells in the vertical direction. The distribution of cells is vertically nonuniform, with 150 cells in the upper 150 km, 10 cells in the following 50 km, and 120 cells in the remaining 1,200 km. Consequently, the horizontal resolution is 3 km, and the vertical resolution is 1 km in the lithosphere and 10 km in the sublithospheric domain, respectively. Tests with higher and lower spatial resolution gave consistently similar results.

We do not attempt to resolve subduction initiation processes, and subduction is initialized by introducing a 10 km wide strain-weakened zone composed of a sediment wedge in the oceanic lithosphere at the ocean-continent boundary. To establish a similar subduction interface for all models, each model has the same 3 Myr long subduction initiation phase. During this phase, the oceanic lithosphere is pushed with 5 cm/yr, the continent is not moving, and the continental lithospheric mantle is “strong” over the whole continental domain.

### 2.3. Parameter Variations in the Models Presented

With a set of 10 models (Figure 2), we test the effect of backarc lithospheric strength and absolute plate velocities on overriding plate strain regime in ocean-continent subduction systems. Models M1 to M4 are described in detail with several time steps, while models M5 to M10 are summarized with their final configuration (Figure 7). Key viscosity plots of models M1–M4 are shown in Figures S1 and S2. The free-surface evolution of all models is presented in Figure 8, and an animation of every model is uploaded to a data repository (see Acknowledgements). Four additional models related to M3 and M4 (M4b, M4c, M3_1000, and M4_1000) are in supplementary Figures S4 and S5.

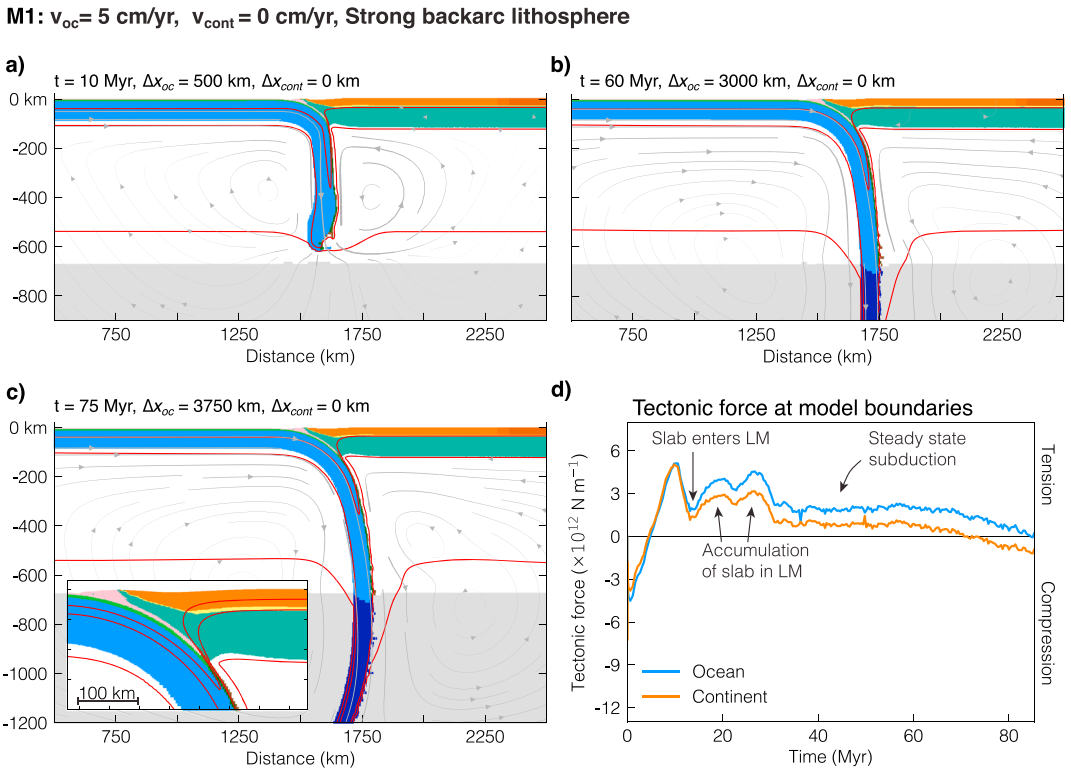


**Figure 3.** Reference model (M1) with a neutral overriding plate strain regime. (a–c) Material colors (see Figure 1) with isotherms (550, 1,330, and 1,500 °C) and streamlines scaled in thickness to velocity. t is model time, and $\Delta x_{oc}$ and $\Delta x_{cont}$ are the amounts of oceanic and continental convergence. (c) Inset contains zoom with additional isotherm at 350 °C. (d) Tectonic forces (integrated horizontal deviatoric stresses). LM is abbreviation for lower mantle. See Movie S1 for a model animation.

The models are driven by velocity boundary conditions and do not account for mid-oceanic ridge(s), lateral temperature and viscosity variations, neighboring plates, or large-scale convective drag. To better understand model behavior and to see whether model evolution is Earth-like, we track the tectonic boundary force (see supporting information S1 for more information about its computation) in the lithosphere at the model domain boundaries (Butler & Beaumont, 2017). An in-depth assessment of the forces acting during model evolution is given in section 4.

## 3. Results

### 3.1. M1: Reference Model

The reference model M1 has a subducting plate velocity of 5 cm/yr, a fixed upper plate, and a strong backarc lithospheric mantle with the same viscosity throughout the whole model domain (Figures 3 and 8a).

The first phase of subduction is characterized by initial localization of deformation along the weak interface. After 5 Myr, the slab steepens and subducts vertically through the upper mantle until ~12 Myr, when it enters the lower mantle. After a phase of slab accumulation and bending in the lower mantle (15 to 35 Myr, see also Movie S1), the subduction zone enters steady-state subduction, characterized by a steep slab that shows no interaction with the transition zone. Two whole model scale poloidal flow cells form on both sides of the slab (Figure 3c). The position of the trench is not changing during the model run, and the free surface is steady (Figure 8a).

The model evolution is reflected in the development of the boundary forces (Figure 3d). Initial convergence is associated with compressive tectonic forces in both plates. From 5 Myr, the boundary forces in both plates are tensional and reach their maximum at ~10 Myr, right before the slab reaches the lower mantle. Tectonic stresses drop once the slab enters the lower mantle followed by relatively constant and small ($< 3 \times 10^{12}$ N/m) tectonic boundary forces during steady-state subduction.

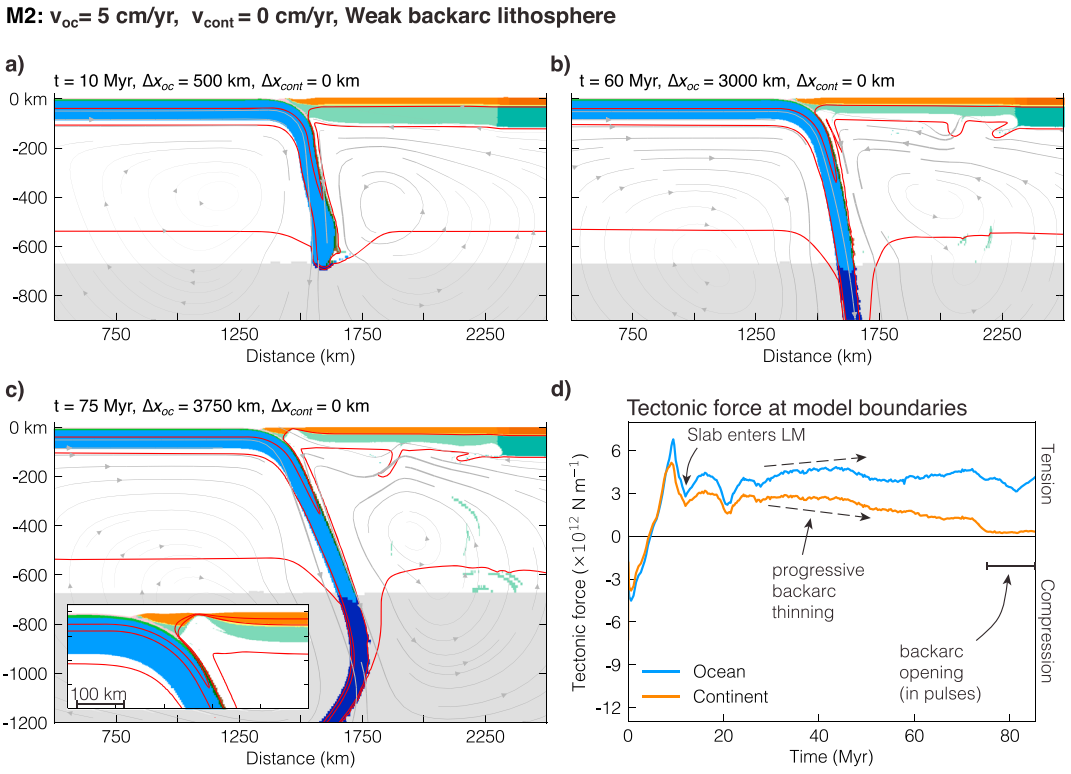


**Figure 4.** M2 showing backarc spreading. (a–c) Material colors (see Figure 1) with isotherms (550, 1,330, and 1,500 °C) and streamlines scaled in thickness to velocity. t is model time, and $\Delta x_{oc}$ and $\Delta x_{cont}$ are the amounts of oceanic and continental convergence. (c) Inset contains zoom with additional isotherm at 350 °C. (d) Tectonic forces (integrated horizontal deviatoric stress). LM is abbreviation for lower mantle. See Movie S2 for a model animation.

### 3.2. M2: Weak Backarc Lithospheric Mantle

Model M2 has the same velocity boundary conditions as M1 but a weak backarc lithospheric mantle with identical compositional density and rheology as the underlying sublithospheric mantle (Figures 4 and 8b).

After subduction initiation and before the slab enters the lower mantle (between 7 and 10 Myr), a short phase of trench retreat results in pure shear thinning of the weak continental lithosphere (see Movie S2), accompanied by moderate slab shallowing (Figures 4a and 8b). During ongoing subduction, two model scale poloidal flow cells form on both sides of the slab. The resulting subhorizontal shear flow of the sublithospheric mantle at the base of the backarc lithosphere evokes small thermal and mechanical perturbations which develop into Rayleigh-Taylor instabilities leading to convective thinning of the backarc mantle lithosphere in the weak domain (10 to 60 Myr). With ongoing subduction, corner flow induces increased thinning of the mantle lithosphere about 150 km landward from the trench (Figure 4b) ultimately resulting in backarc rupture at around 75 Myr with a 150 km wide block that is rifted off the overriding plate (Figure 4c). Backarc opening and associated trench retreat are faster than slab retreat in the lower mantle, and the slab dip decreases until the slab bends inward at around 400 km depth, inducing a back and forward movement of the slab. Repeated folding of the slab is associated with pulse-like backarc opening with a recurrence time of ~10 Myr (Figure 8b and Movies S1–S6). Convective thinning of the backarc lithospheric mantle leads to conductive heating and an increase of surface heat flow > 60 mW/m$^2$.

### 3.3. M3: Overriding Plate Movement Toward the Trench, Strong Backarc Lithospheric Mantle

Model M3 has a subduction velocity of 5 cm/yr, a trenchward overriding plate velocity of 2 cm/yr, and a strong backarc continental lithospheric mantle (Figures 5 and 8c). Note that the backarc crust is weaker than the strong "cratonic" crust (e.g., Figure 1).

During the first 10 Myr, the slab sinks relatively vertical through the upper mantle and reaches the lower mantle transition zone with an almost vertical angle. Further overriding plate movement leads to slab flattening, as the trench retreats faster than the slab sinks into the lower mantle. Slab bending at 20 and 40 Myr

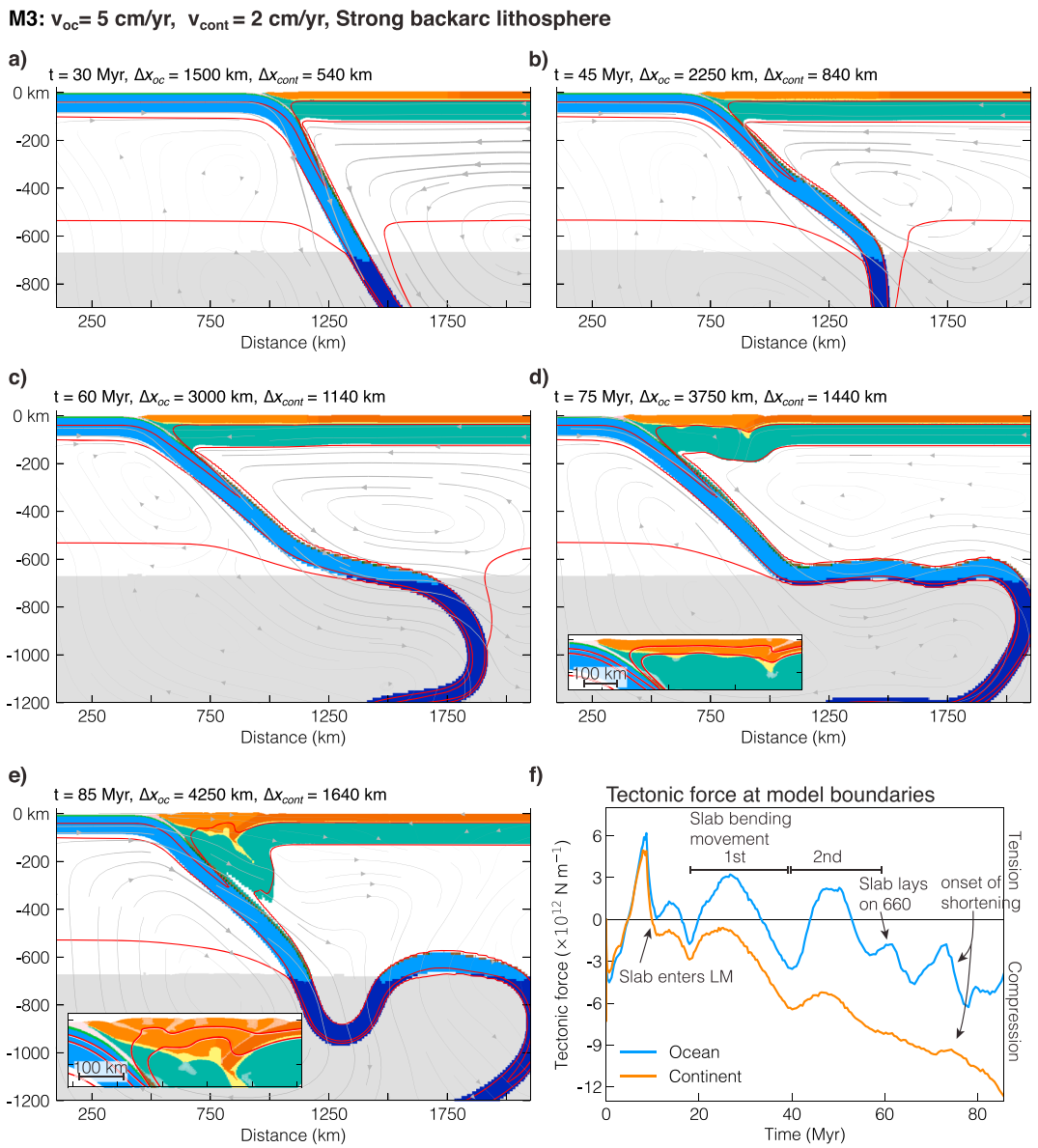


**Figure 5.** M3 showing underthrusting of the cratonic region and overriding plate shortening. (a–e) Material colors (see Figure 1) with isotherms (550, 1,330, and 1,500 °C) and streamlines scaled in thickness to velocity. t is model time, and $\Delta x_{oc}$ and $\Delta x_{cont}$ are the amounts of oceanic and continental convergence. (d,e) Inset contains zoom with additional isotherm at 350 °C. The white overlay highlights strain-weakened shear zones. (f) Tectonic forces (integrated horizontal deviatoric stress). LM is abbreviation for lower mantle. See Movie S3 for a model animation.

induces minor back and forward slab movements, as in M2, linked with slab advance in the lower mantle and slab stagnation in the transition zone (Figure 5c). After 70 Myr, the backarc continental lithosphere fails through large-scale folding followed shortly after (at 75 Myr) by underthrusting of the strong cratonic crust (Figure 5e). Subsequently, significant trench advance is associated with ablative subduction and backarc lithospheric mantle shearing off from the overriding crust (Figure 8c).

The boundary forces show the different stages of model evolution (Figure 5f). The two slab bending events are reflected in periodic increase and decrease of boundary forces between 20 and 60 Myr. Further trench retreat leads to an increase in boundary forces until shortening, and subsequent mountain building of the backarc continent results in a very high continental boundary force exceeding $9 \times 10^{12}$ to $12 \times 10^{12}$ N/m. Supplementary model M3_1000 (Figure S5) with an extended ocean has a very similar model development, showing that overriding plate shortening is not induced by approaching the left model boundary.

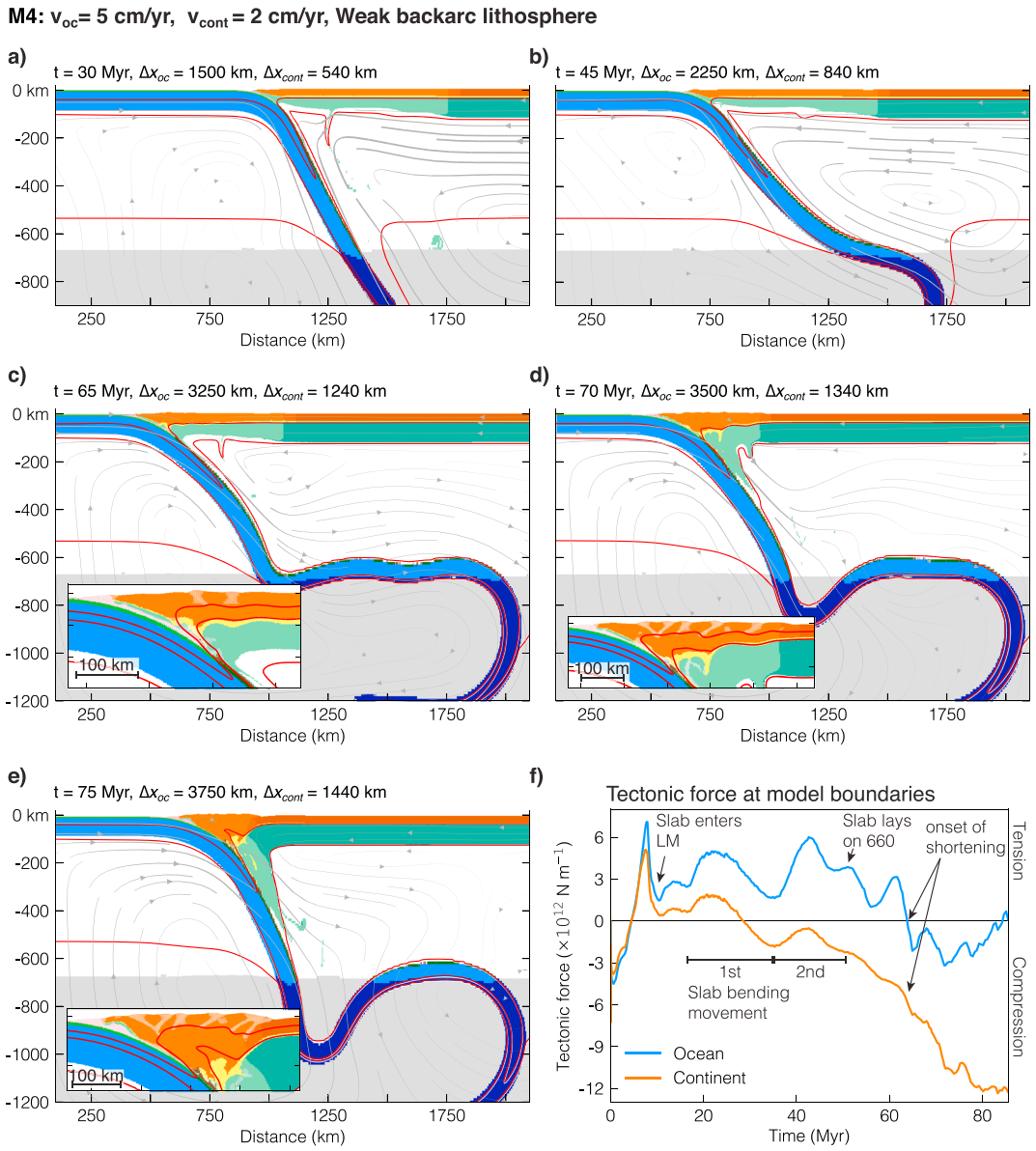


**Figure 6.** M4 showing overriding plate shortening through failure of the weak backarc lithosphere. (a–e) Material colors (see Figure 1) with isotherms (550, 1,330, and 1,500 °C) and streamlines scaled in thickness to velocity. t is model time, and $\Delta x_{oc}$ and $\Delta x_{cont}$ are the amounts of oceanic and continental convergence. (c–e) Inset contains zoom with additional isotherm at 350 °C. The white overlay highlights strain-weakened shear zones. (f) Tectonic forces (integrated horizontal deviatoric stress). LM is abbreviation for lower mantle. See Movie S4 for a model animation.

### 3.4. M4: Overriding Plate Movement Toward the Trench, Weak Backarc Lithospheric Mantle

Model M4 has the same velocity boundary conditions as M3 but a weak backarc lithospheric mantle (Figures 6 and 8d).

During the first 10 Myr, before the slab interacts with the lower mantle, trench retreat exceeds the overriding plate velocity resulting in pure shear thinning of the backarc lithosphere and a slight shallowing of the slab similar to M2. Subsequent model evolution is governed by the interplay between backarc weakening through convective thinning and slab anchoring in the lower mantle. Corner flow enhances convective removal and weakening of the lithospheric mantle 150 km landward of the trench. Similar to M3, the interaction between slab folding and differential velocities of the trench and the slab in the lower mantle result in two back and forth movements of the slab, after which the slab lays down on the mantle transition zone (Figure 6b). Further overriding plate movement toward to trench leads to shortening of the continent after 65

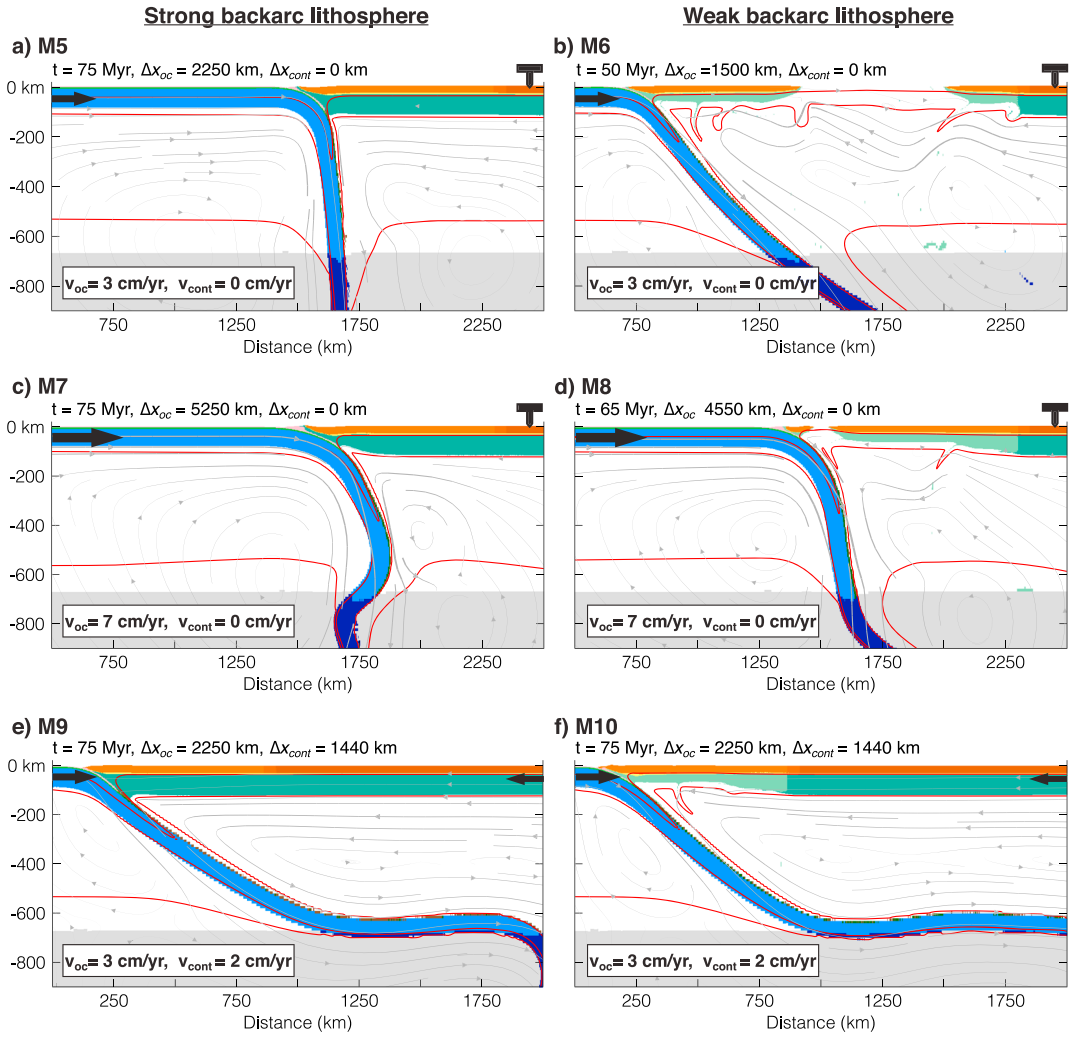


**Figure 7.** M5–M10 sensitivity to different plate velocities. M5, M7, M9, and M10 have a neutral overriding plate strain regime, while M6 and M8 show backarc spreading. (a–f) Material colors (see Figure 1) with isotherms (550, 1,330, and 1,500 °C) and streamlines scaled in thickness to velocity. t is model time, and $\Delta x_{oc}$ and $\Delta x_{cont}$ are the amounts of oceanic and continental convergence.

Myr (Figure 6c). Crustal thickening and mountain building starts near the plate interface and migrates from there inland (Figure 6d), as the continental lithospheric mantle is initially the thinnest at the trench. The first fault zone nearest to the trench separates a marginal block from the rest of the mountain belt, related to deflection of the temperature field. During subsequent shortening, the remaining lithospheric mantle is ablatively subducted. The trench advances until the cratonic lithosphere thrusts under the evolving mountain belt blocking further shortening, followed by trench retreat with approximately the same velocity as the overriding plate (Figure 8d). Mountain building is completed within 20 Myr.

Similar to M3, the tectonic boundary forces record two slab bending movements between 20 and 50 Myr. Further overriding plate movement induces increasing compressional stresses in the continental plate resulting in shortening once the compressive forces are $>5 \times 10^{12}$ N/m. Supplementary model M4_1000 (Figure S5) with an extended ocean has a very similar model development as M4, showing that overriding plate shortening is not induced by approaching the left model boundary.

### 3.5. Sensitivity to Different Plate Velocities

Models M5 to M10 (Figure 7) comprise three model pairs where we test the effect of different plate velocities on the overriding plate strain regime. Each set of models consists of one model with a strong and one model with a weak backarc lithospheric mantle.

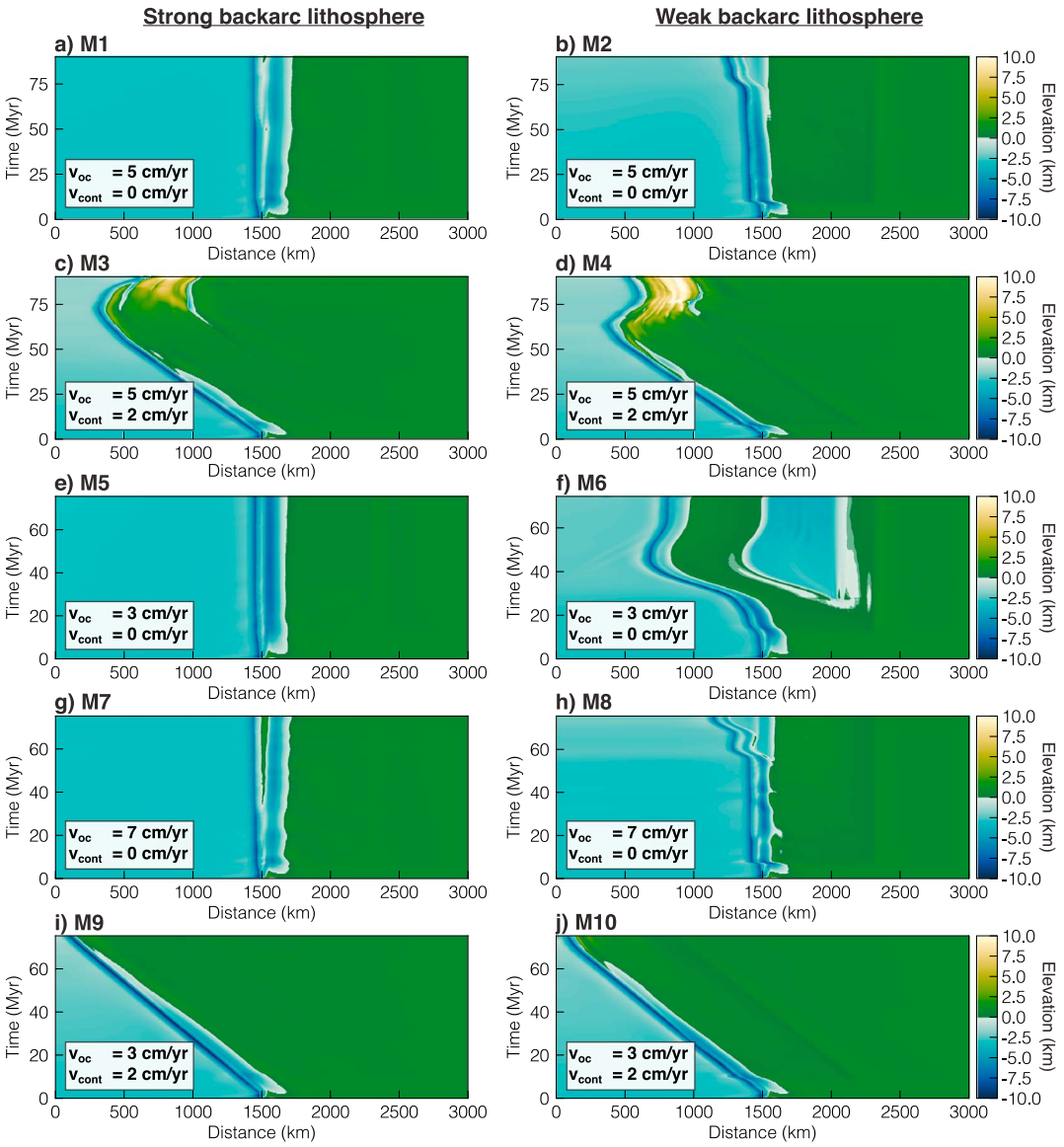


**Figure 8.** Evolution of free-surface elevation of models M1–M10. The colorbar is the same for all models, and the continental side boundary is assumed to be stable at 800 m above sea level. Note the pulse-like backarc opening in models 2, 6, and especially 8. Note also that onset of shortening in M3 starts in the continent, while shortening in M4 begins near the trench and migrates inland.

Models M5 and M6 have a low subduction velocity of 3 cm/yr and zero overriding plate velocity. In case of the strong continental mantle (M5), subduction is stable, and the overriding plate does not deform (Figures 7a and 8e). In model M6, the weak backarc lithosphere develops convective thinning in a similar fashion to M2. However, backarc extension occurs earlier than in M2 after 28 Myr of model evolution. Additionally, convective thinning further inland leads to necking significantly offset from the trench by >500 km. The post-opening retreat of the trench and continental block is very rapid (5 cm/yr) until the slab has reached a shallow dip angle and large amount of slab material has accumulated in the lower mantle (45 Myr). Subsequent slab steeping is accompanied by a short phase of trench advance followed by stationary subduction (Figure 8f and Movies M5 and M6).

Models M7 and M8 have a high subduction velocity of 7 cm/yr and zero overriding plate velocity. M7 and M8 have the same relative convergence velocity as models M3 and M4. They do, however, not exhibit overriding plate shortening but result in a very similar behavior as M1 and M2, with overriding plate extension if the overriding lithospheric mantle is weak (M7). The subduction velocity of 7 cm/yr induces more slab bending

movement in the upper mantle compared to models with a subduction velocity of 5 cm/yr. The tectonic forces at both plate boundaries vary between $-2\times10^{12}$ and $4\times10^{12}$ N/m during model evolution (Figure S3).

Models M9 and M10 have a low subducting plate velocity of 3 cm/yr and an overriding plate velocity of 2 cm/yr. Hence, M9 and M10 have the same relative convergence velocity as models M1 and M2. Nevertheless, they do not show overriding plate extension but a neutral strain regime throughout the whole model evolution. In both models, trench retreat occurs at the same velocity as overriding plate movement, with the slab laying down in the transition zone after 50 to 60 Myr of model evolution.

## 4. Analysis of Forces Driving Model Evolution

Subduction and model evolution are guided by the balance of slab pull and a number of counteracting forces. Because of the dynamic nature of the models, it is not possible to develop an analytical force balance solution for model development. However, to better understand model evolution, it is useful to consider the magnitude of different forces acting during subduction.

### 4.1. Driving Force: Slab pull, $F_{sp}$

The only internally developing force driving subduction in the models is slab pull ($F_{sp}$), which is a result of the thermal anomaly and density difference of the subducting slab. In the models presented here, the negative density of the slab is on average 60 kg/m$^3$. The resulting slab pull is increasing with slab length to $2.5\times10^{13}$ N/m before the slab enters the lower mantle and reaches a maxium of $4.5\times10^{13}$ N/m during whole model subduction.

### 4.2. Resisting Forces

Several resisting forces dissipate the gravitational potential energy of the slab pull: shear resistance at the interface ($F_{int}$), viscous drag in the upper and lower mantle ($F_{vd} = F_{um} + F_{lm}$), buoyancy related to the negative Clapeyron slope of the upper- to lower-mantle phase change ($F_{660}$), slab suction ($F_{suc}$), and internal deformation of the slab ($F_{def}$).

#### 4.2.1. $F_{int}$

The dominantly frictional subduction interface reaches down to the backarc lithosphere-asthenosphere boundary ($z_{lab}$) and can be approximated by its integrated frictional strength:

$$F_{int} = \int_0^{z_{lab}} \sigma'_{plast}(z)dz = \frac{1}{2}\rho g z_{lab}^2 \sin(\phi_{eff}) + C z_{lab}\cos(\phi_{eff}). \quad (6)$$

For models with a strong backarc, $z_{lab}$ is not changing considerably during model evolution and reaches down to 120 km, with $F_{int}(120\,km) \approx 8\times10^{12}$ N/m. In case of a weak backarc, thinning of the mantle lithosphere results in an elevated lithosphere-asthenosphere boundary with values of $F_{int}(80\,km) \approx 4\times10^{12}$ N/m and $F_{int}(40\,km) \approx 1\times10^{12}$ N/m.

#### 4.2.2. $F_{vd}$

The viscous shear resistance of the mantle on the sides of the slab is difficult to assess, since there is no fixed length scale for the boundary layer accommodating the shear. Inferring an average length scale ($w$) from the forward models, we can express the viscous shear force as (Billen, 2008)

$$F_{vd} = \frac{2v}{w}\mu L = \frac{2v}{w}(\mu_{um}L_{um} + \mu_{lm}L_{lm}), \quad (7)$$

where v is subduction velocity, $L$ is slab length, $\mu$ is effective viscosity in the upper mantle (um) and lower mantle (lm), and $v$ is velocity. An effective viscosity of $\mu_{um} = 1\times10^{19} - 1\times10^{20}$ Pa s, and average $w = 100$ km, in the vicinity of the slab leads to an upper mantle viscous drag two orders of magnitude less than slab pull and therefore negligible. Viscous drag at base of plates is similarly not significant in our models, because potentially high strain rates lead to very low viscosities of $\mu_{um} = \sim 1\times10^{19}$ Pa s within a similar length scale $w = \sim$100 km. Viscous shearing in the lower mantle, however, requires a considerable force in the order of slab pull. For instance, a 400 km long slab with a sinking velocity of 5 cm/yr, $w = 100$ km, and $\mu_{lm} = 3\times10^{21}$ Pa s induces a shear resistance of $F_{lm} = 2\times10^{13}$ N/m, almost half of the maximum slab pull.

#### 4.2.3. $F_{660}$

The positive buoyancy force added by the negative Clapeyron slope of the lower mantle phase transition is in the order of 2–$4\times10^{12}$ N/m in case of straight slab penetration through the transition zone. Models 3, 4, 9, and 10 show that a shallower subduction angle can lead to foundering in the transition zone, which leads to

a much larger positive buoyancy force. $F_{660}$ is therefore highly variable and can have a significant influence on slab evolution in the transition zone. Agrusta et al. (2017) show that the Clapeyron slope of the phase transition has a large impact on slab foundering, where a steeper negative slope enhances slab stagnation.

#### 4.2.4. $F_{suc}$

Slab suction is an upward-directed force for shallow dipping slabs ($\lessapprox 30°$, Stevenson & Turner, 1977) and can be the cause of flat slab subduction during the subduction initiation phase (Rodriguez-Gonzalez & Negredo, 2012; Huangfu et al., 2016). The models presented here do not develop flat slab subduction, as the average upper mantle slab dip during model evolution is never less than 45°, resulting in a negligible suction force $F_{suc} < 3 \times 10^{11}$ N/m.

#### 4.2.5. $F_{def}$

Following Conrad and Hager (1999) and Funiciello et al. (2003), the internal deformation of a plate in terms of viscous bending can be approximated by

$$F_{bending} \approx v \mu_{eff} \frac{h^3}{r^3}, \tag{8}$$

where $\mu_{eff}$ is effective viscosity, $h$ is plate thickness, and $r$ is the bending radius. Assuming that slab bending induced deformation occurs at several locations $F_{def} = n \times F_{bending}$. This will typically lead to values of $F_{def} = 5 \times 10^{11}$–$5 \times 10^{12}$ N/m, in the order but lower than the shear resistance at the interface ($F_{int}$). $F_{def}$ increases when the overriding plate also deforms.

### 4.3. Summary of Forces

The main forces resisting slab pull ($F_{sp}$) are viscous drag in the lower mantle, shearing of the subduction interface, internal lithospheric deformation, and the dynamically changing buoyancy force of the phase transition in the transition zone. Another force visible in the tectonic boundary forces of M3 and M4 is the gravitational stress exerted by rising topography ($F_{topo}$). A 3 km high mountain belt exerts a force of $3 \times 10^{12}$ to $4 \times 10^{12}$ N/m onto its foreland (Stüwe, 2007), while a 6 km high mountain range with a 70 km thick crust exerts a force of $8 \times 10^{12}$ to $9 \times 10^{12}$ N/m.

Summarizing, the tectonic boundary force ($F_{TBF}$) can be approximated as a combination of

$$F_{TBF} \approx F_{sp} - \left(F_{lm} + F_{int} + F_{def} + F_{660} + F_{topo}\right). \tag{9}$$

In all our models, except during later stages of mountain building models M3 and M4, the absolute resulting tectonic boundary forces have the same magnitude as ridge push (see Figure S3), which is in the order of $3 \times 10^{12}$ (to $7 \times 10^{12}$) N/m (Parsons & Richter, 1980; Turcotte & Schubert, 1982). This shows that model evolution is Earth-like. In nature, subduction zone mountain belts are expected to be self-limiting in their behavior and will either not reach the later stages of our models (M3, M4, M4c, and M4b) or exhibit slow down of the overlying plate. Basal drag associated with large-scale poloidal flow in addition to buoyant upwellings could provide additional forces driving mountain building as proposed for the Andes (Husson et al., 2012; Faccenna et al., 2017). The evolution of boundary forces can also be interpreted as a measure of how much the plates need to be pushed or pulled in order to obtain the given velocity boundary conditions. For instance, the tensional stress peak in all models around 10 Myr and also the slab bending movements in M3 and M4 coincide with plate acceleration and deceleration phases in free subduction models (Agrusta et al., 2017; Capitanio et al., 2010; Funiciello et al., 2004; Garel et al., 2014).

Our force balance analysis shows that the forces driving and resisting subduction are in the same order of magnitude and result only in a small absolute surplus to deform the overriding plate. Therefore, a weak backarc is crucial for extension or shortening of the overriding plate, as discussed in the next section.

## 5. Mode Selection of Overriding Plate Deformation

With our small set of models, we can reproduce overriding plate extension or shortening in ocean-continent settings and show that deformation is primarily controlled by the strength of the backarc lithospheric mantle and the absolute plate velocities of the subducting and overriding plate (Figure 9). In the following three subsections, we will discuss in depth the role of these primary controlling factors.

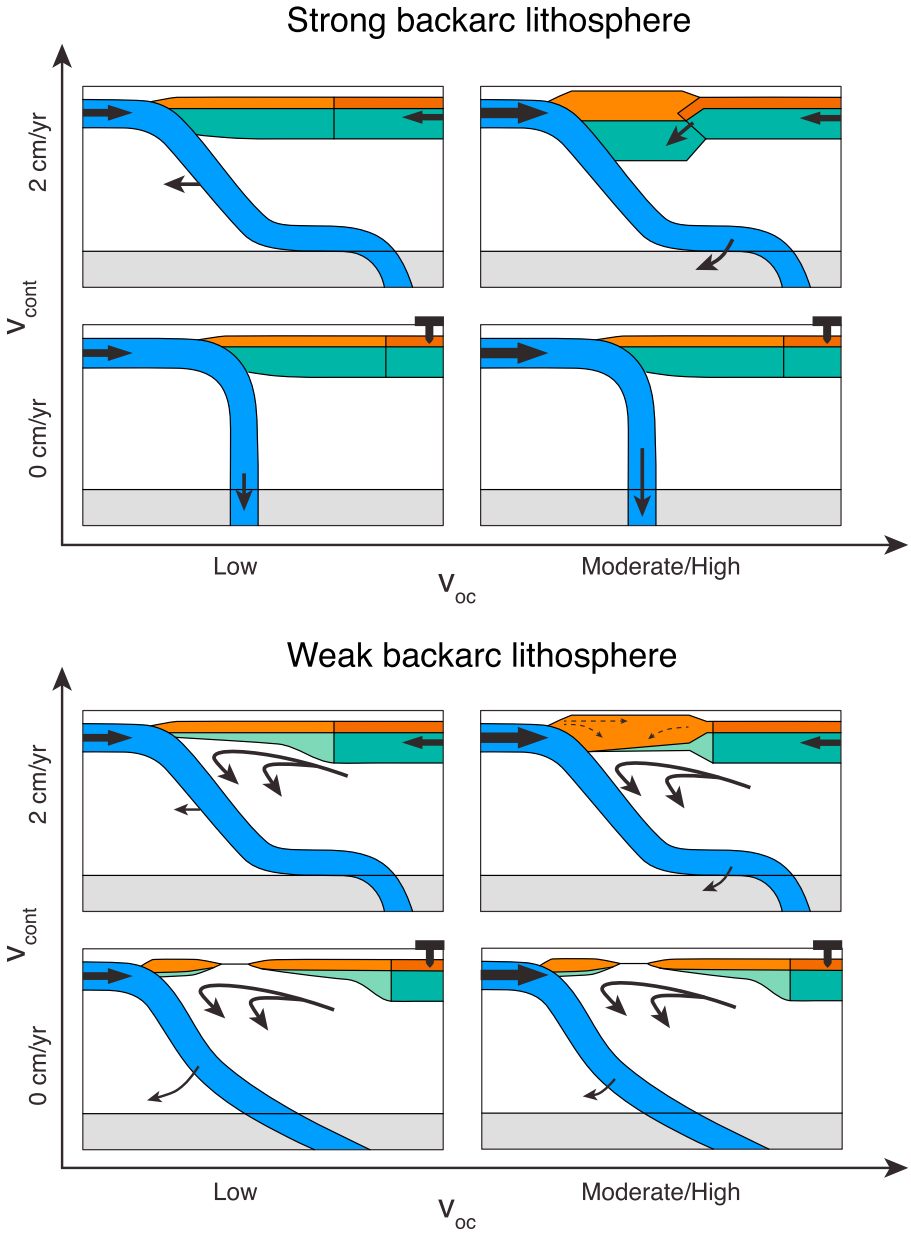


**Figure 9.** Summary of model behavior as a function of lithospheric strength (upper and lower panels), the subduction velocity ($v_{oc}$), and the overriding plate velocity ($v_{cont}$). The models with a strong backarc lithospheric mantle have a neutral overriding plate strain regime, unless the subduction velocity is high and the overriding plate moves toward the trench (M3). This situation leads to overriding plate shortening through underthrusting of the strong cratonic hinterland. A weak backarc lithosphere will be removed through gravitational instabilities, which can induce backarc spreading independent of the subduction velocity, but only if the overriding plate does not move toward the trench. When slab sinking is balanced by a low subduction velocity and an overriding plate which moves toward the trench, then the strain regime is neutral. If the subduction velocity is increased, the overriding plate shortens.

### 5.1. The Influence of Backarc Lithospheric Strength

To first order, the backarc will deform if the net tectonic driving force is larger than the plate's integrated strength. The strength of the backarc lithospheric mantle is therefore pivotal in determining whether the overriding plate can extend and how it shortens (Figure 9). Continental lithosphere with a strong mantle has an integrated strength of $\sim 9 \times 10^{12}$ N/m, while the strength of lithosphere with a weak mantle not yet affected by thinning is $\sim 5{\times}10^{12}$ N/m. Convective thinning and removal of weak backarc mantle lithosphere results in additional weakening to a minimum strength of $3{\times}10^{12}$ N/m. Removal of the backarc lithosphere

also reduces the length of the subduction interface, lowering the interface resistance and increasing the net pull exerted by the slab. The combination of lithospheric thinning, thermal weakening, and subduction interface shortening enables backarc extension. In case of even weaker backarc mantle, extension and backarc opening is likely to occur shortly before the slab interacts with the lower mantle, shown by tensional stress peaks around 10 Myr in all models.

Overriding plate shortening is possible with and without a weak backarc lithospheric mantle. In case of strong backarc lithosphere (as in model M3), the tectonic driving forces in the overriding plate need to exceed the high integrated strength of $9 \times 10^{12}$ N/m, while for a weak backarc lithospheric mantle (as in model M4), onset of shortening occurs when the driving force is in the order of $\sim 5 \times 10^{12}$ N/m. Supplementary models M4b and M4c test the sensitivity to overriding plate velocity (M4b) and enhanced backarc mantle lithosphere weakening (M4c; Figure S4). M4b with a lower overriding plate velocity results in shortening at $\sim 4 \times 10^{12}$ N/m, similar to M4, while model M4c with an even weaker lithospheric mantle (wet Olivine*0.5, Figure S4) exhibits enhanced lithospheric removal, inducing earlier shortening at a lower initial tectonic boundary force of $\sim 3 \times 10^{12}$ N/m. These models show that onset of shortening in subduction zones with a weak and partially removed backarc lithospheric mantle does not require a significant tectonic force in addition to ridge push. Kelly et al. (2016), Krystopowicz and Currie (2013), and Z. H. Li et al. (2016) show in continent-continent collision models that large amounts of backarc lithospheric mantle can be removed, similar to M3. Models presented here indicate that this requires a large tectonic force and may provide a viable mechanism for systems that are shortening but is unlikely to induce backarc opening.

### 5.2. Influence of the Subduction Velocity $v_{oc}$

The results presented here indicate that the velocity of the subducting plate may provide a secondary control on overriding plate extension. However, the model results suggest that it must be larger than 3 cm/yr for overriding plate shortening to occur (Figure 9). The impact of the subduction velocity can be best understood in the context of the slab's natural sinking velocity ($v_{sink}$), considering that the slab will exert a tensional force onto the overriding plate if $v_{oc}$ is smaller than $v_{sink}$. Accordingly, overriding plate extension occurs earliest in M6, where $v_{oc}$ is the smallest ($v_{oc} = 3$ cm/yr). Interestingly, overriding plate extension occurs earlier in M8 ($v_{oc} = 7$ cm/yr) than in M2 ($v_{oc} = 5$ cm/yr). This is most likely related to faster removal of the backarc lithosphere through faster corner flow in front of the slab.

### 5.3. Influence of the Overriding Plate Velocity $v_{cont}$

The overriding plate velocity plays a critical role in determining overriding plate deformation (Figure 9) and is linked to slab anchoring in the lower mantle. If trench retreat resulting from overriding plate motion toward the trench is faster than slab retreat in the lower mantle, the slab dip decreases, and the subduction system favors overriding plate shortening and suppresses extension. This is illustrated by model M10, which does not exhibit overriding plate extension although the cumulative convergence velocity is 5 cm/yr and, hence, the same as in M2. All models with backarc extension show that backarc opening is not a continuous process but occurs episodically without changing the boundary conditions (Figure 8). This is also caused by periodic slab dip flattening during fast trench retreat.

Overriding plate shortening occurs when it is moving toward the trench and when the net convergence velocity is larger than the average slab sinking and retreat velocity in the lower mantle. Both M3 and M4 exhibit slab foundering in the lower mantle transition zone before overriding plate shortening. Supplementary model M4b with a lower $v_{cont}$ of 1 cm/yr (Figures S4a and S4b) shows that slab foundering is not required for overriding plate shortening.

Conversely, slab anchoring in the lower mantle enhances overriding plate extension, if the overriding plate moves away from the trench. However, extension would in this case require a weak and thin lithospheric mantle, as a strong backarc has a greater strength than the subduction interface.

The analysis of driving and resisting forces shows that slab anchoring is largely related to the large viscous drag in the lower mantle. However, also volumetric considerations which are not captured by the force analysis may play an important role. The slab is separating two poloidal flow cells with only limited exchange of material at the bottom of the model domain. Mass conservation of the two flow cells leads to slab flattening in response to trench retreat, and vice versa, and enhances a stable position of the slab in the lower mantle.

### 5.4. Model Limitations

Our models are a simplified representation of nature, and there are several processes we do not account for including most notably 3-D aspects of subduction systems, the role of water and fluid flow, variable oceanic plate age, stronger or weaker continental rheology, and more comprehensive mantle phase changes.

Toroidal (i.e., horizontal) return flow around the slab edge may have a significant influence on subduction dynamics. A short slab edge distance facilitates return flow and may enhance slab retreat, while zones far away from subduction edges cannot so easily retreat and favor a stable position (Funiciello et al., 2004; Schellart et al., 2007; Schellart, 2008). The models presented here are 2-D and do not include toroidal flow and may be taken to represent the center of large subduction zones. Toroidal return flow is expected to lead to reduced slab anchoring and promote overriding plate extension. Accordingly, higher subduction and or overriding plate velocity is required in order to obtain overriding plate shortening. Similarly, subducting lithosphere with a larger or smaller negative buoyancy will shift the set of models toward more extension in case of a heavier plate or more shortening in case of a lighter subducting plate.

Another 3-D effect which we do not capture is how adjacent collision of two continental blocks may influence the stress regime and facilitate backarc opening (Magni et al., 2014; Moresi et al., 2014).

Mountain building models M3 and M4 show ablative subduction of the backarc lithospheric mantle during the later stages of mountain building, resulting from viscous coupling at the plate interface. Fluids derived from the subducting slab may weaken the subduction interface at depth for natural systems and may inhibit ablative subduction (Arcay et al., 2005; Faccenda et al., 2012; Gorczyk, Gerya, et al., 2007, Gorczyk, Willner, et al., 2007). We note, however, that ablative subduction has been proposed to explain the formation of a mountain belt on top of a subduction zone (Pope & Willett, 1998).

We tested the influence of a weaker or stronger rheology of the overriding plate crust, and although showing some differences in timing of deformation and mountain belt structure, the overall behavior is similar. Fluids and (fluid induced) melting may have a strong weakening effect on the continental lithosphere and possibly also on the subduction interface. A melt-weakened lithospheric mantle would possibly be even weaker than in our models, enhancing lithospheric removal leading to earlier backarc extension and shortening (Figure S4).

Our models do not account for latent heat of phase changes, viscous dissipation, and more complex and variable phase changes in the upper and lower mantle. Further studies could include those and investigate their effect on the overriding plate strain regime.

### 5.5. Comparison With Natural Systems

We next proceed with comparing the inferred controls on the mode of overriding plate deformation with observations from natural systems. The Tonga, Scotian, and the Mediterranean subduction zones with extensive backarc spreading activity have a very low (<1 cm/yr) absolute overriding plate velocity perpendicular to the trench in common (O'Neill et al., 2005; Schellart et al., 2008). This is consistent with model inference which indicates that backarc spreading requires that the overriding plate does not move toward the trench. The (central) Andes in contrast are the only area with major recent overriding plate shortening in an ocean-continent subduction setting (Schellart et al., 2007). Here the overriding South American plate moves toward the trench with 1–2 cm/yr, and the oceanic Nazca plate subducts with 6–7 cm/yr (O'Neill et al., 2005; Schellart et al., 2008). This velocity configuration is also consistent with the model predictions presented here. Below we investigate in detail the role of subduction dynamics at depth and the influence of backarc lithospheric strength for the central Andean and the Hellenic subduction zones (Figure 10).

Oceanic subduction below the central Andes started in the Jurassic and induced backarc extension within the stable overriding plate during most of the Mesozoic (Armijo et al., 2015; Charrier et al., 2007; Coira et al., 1982; Horton, 2018). The main shortening phase started around 50 Ma (Armijo et al., 2015; Barnes & Ehlers, 2009; Oncken et al., 2006), following some earlier local shortening around 100 Ma (Arriagada et al., 2006; Coira et al., 1982; Horton, 2018). Phases of extension and shortening have been attributed to absolute velocity changes of the overriding plate (Horton, 2018; Maloney et al., 2013), with inception of the main shortening phase coinciding with plate reorganization in the Pacific around 50 Ma (e.g., Seton et al., 2012; Torsvik et al., 2010; Wessel et al., 2006). Shortening started in the west and progressed landward (Horton, 2018; Oncken et al., 2006), leading to underthrusting of the Brazilian shield and bivergent orogenic growth during the last 10 Myr (Armijo et al., 2015; Oncken et al., 2006). A rigid "marginal" block offsets deforma-

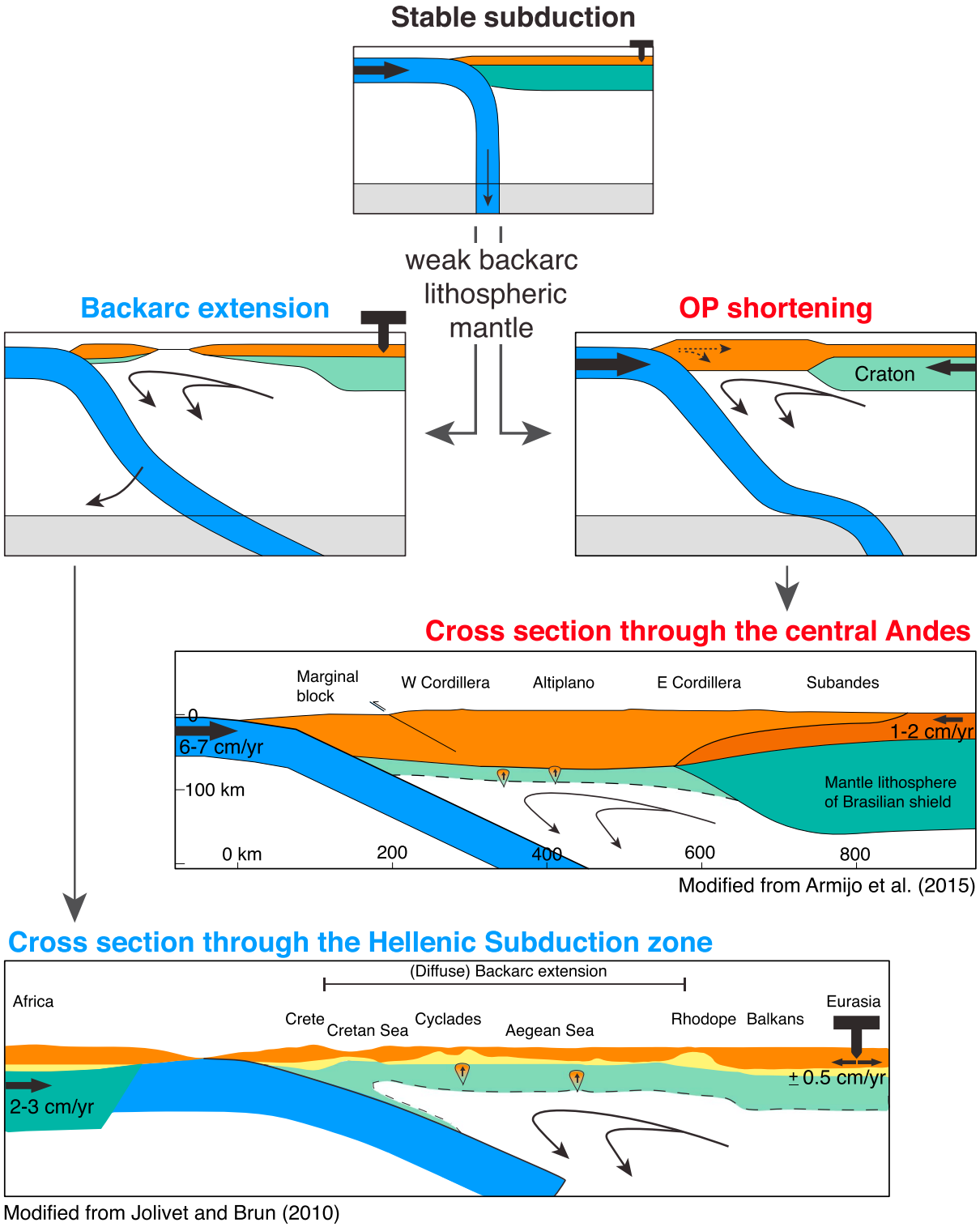


**Figure 10.** Cartoon and two natural examples showing the parameters which are needed to go from stable subduction to backarc extension or overriding plate shortening. Backarc extension requires an overriding plate which is not moving toward the trench and a weak backarc lithospheric mantle which is removed through gravitational instabilities. This situation matches with the plate tectonic configuration in the Hellenic subduction zone, where oceanic lithosphere associated with the African plate slowly subducts under the more or less stable Eurasian continent. A removed lithospheric mantle and thickened continental crust led to diffuse backarc extension with lower crustal flow (yellow material) during the last 35 Ma (Faccenna et al., 2014; Jolivet et al., 2013). Overriding plate shortening requires the overriding plate to move toward the trench and is facilitated by a removed lithospheric mantle. This is the case for the central Andes, where the South American plate is moving toward the trench against the subducting Nazca plate. The strong marginal block as well as progression of shortening landward (Armijo et al., 2015; Horton, 2018; Lamb, 2011; Oncken et al., 2006) can be explained by our models with a removed lithospheric mantle.

tion approximately 200 km from the trench into the hinterland throughout the shortening phase (Armijo et al., 2015; Lamb, 2011). Orogenic growth and magmatism in the Andes is often interpreted to be associated with delamination of dense backarc lithospheric material (DeCelles et al., 2009; Pelletier et al., 2010; Rapp & Watson, 1995; Wolf & Wyllie, 1993). Seismic tomography indicates very thin backarc lithospheric mantle below the central Andes (Schurr et al., 2006) and landward anchoring of the slab in the lower mantle (Li et al., 2008). Models M4, M4b, and M4c (Supporting Information S1) with overriding plate movement toward the trench and high subducting plate velocity are consistent with the plate velocity framework in the central Andes and show overriding plate strain regimes that compare well with the natural system. Weak backarc lithospheric mantle models with convective thinning (e.g., models M4, M4b, and M4c) exhibit shortening of the overriding plate lithosphere with deformation starting near the trench, landward progression of shortening ending with cratonic underthrusting, matching the evolution of mountain building in the central Andes. Rapid shortening in M4 produces a thicker lithospheric mantle than observed below the central Andes today. Self-limiting growth and slow down of the overriding plate (see section 4.3; M4b, Figure S4), an even weaker backarc lithospheric mantle (M4c, Figure S4), and a thinner lithospheric mantle inherited from preceding backarc extension possibly retained a thin Andean lithospheric mantle during mountain building. Based on the inferred controls on the mode of overriding plate deformation, we suggest that plate reorganizations and the corresponding velocity changes of the South American plate are the main causes of shortening in the Andes. At a crustal scale, the rigid marginal forearc block in the west central Andes may be explained resulting from the low temperatures owing to subduction leading to formation of the first shear zone approximately 200 km landward of the trench (Figures 6 and S4).

The active Hellenic subduction zone is another example that shows the influence of differential velocities on the overriding plate strain regime (Figure 10). Here the northern, oceanic continuation of the African plate subducts under a widely extended backarc region. The current absolute velocity of the African slab is 2–3 cm/yr, and the overriding plate is stable with a velocity of ±0.5 cm/yr (O'Neill et al., 2005; Schellart et al., 2008). Onset of backarc extension is estimated at 35–30 Ma and accelerates at 15 Ma after accretion of a continental block (Faccenna et al., 2014; Jolivet & Brun, 2010). Backarc extension affected thickened crust stacked with continental terranes and a thin, possibly actively delaminating, lithospheric mantle (Altunkaynak & Dilek, 2006; Jolivet & Brun, 2010; Jolivet et al., 2013; Pe-Piper & Piper, 2006). The thick, likely hot, weak crust facilitated middle to lower crustal flow and widespread thinning during rifting in the Aegean (Figure 10). Tomographic models show a moderately dipping slab (45–60°), anchored in the lower mantle (Li et al., 2008; Piromallo & Morelli, 2003; Zhu et al., 2012). Model M6 with a weak and thin backarc mantle and zero overriding plate velocity is consistent with the tectonic context of the Hellenic subduction zone. The subducting slab connected with the large and slowly moving African plate leads to a configuration where the slab's natural sinking velocity is larger than the subduction velocity. Slab pull in the Hellenic case is probably even higher than in our models, as the subducting plate is very old and cold (Müller et al., 2008). These factors in combination with a stable Eurasian plate and a removed lithospheric mantle create a system that strongly promotes backarc extension. The amount of cumulative trench retreat in the Hellenic subduction zone is ~400 km (Faccenna et al., 2014), comparable with model M6, where the slab retreates 500 km within 20 Ma.

## 6. Conclusion

We use thermo-mechanical models to investigate the principal parameters that determine the overriding plate strain regime in an ocean-continent subduction setting and draw the following conclusions.

1. Weak backarc lithospheric mantle, removed through gravitational instability, is required for nature-like deformation of the overriding plate.
2. Strong backarc lithospheric mantle inhibits backarc extension.
3. Owing to slab anchoring in the lower mantle, the absolute and not the relative plate velocities determine whether and how the overriding plate deforms: (a) Overriding plate extension is promoted if the overriding plate is not moving toward the trench. (b) Overriding plate shortening is promoted when the overriding plate moves toward the trench and the subduction velocity is high.
4. The force balance analysis provides an estimate and shows near equilibrium of the driving and resisting forces during subduction. The near equilibrium supports the necessity of a weak overriding plate to deform it.

5. Comparison with the central Andean and Hellenic subduction zones supports the idea that removal of the overriding plate lithospheric mantle and absolute plate velocities determine the overriding plate strain regime.

**Acknowledgments**
This research is supported by TOTAL, through the project "Coupling lithosphere deformation and surface processes (COLORS)." S. W. also acknowledges support from the Research Council of Norway for the project "Subduction zone Water and Metamorphism: A Modelling and Imaging Study" (project 231354). We thank Uninett Sigma2 for computing time of project NN4704K. Two anonymous reviewers and the editors are thanked for very constructive comments that helped to improve the manuscript. Animations of all models can be found under DOI: https://doi.org/10.6084/m9.figshare.8152835.

## References

Agrusta, R., Goes, S., & van Hunen, J. (2017). Subducting-slab transition-zone interaction: Stagnation, penetration and mode switches. *Earth and Planetary Science Letters*, *464*, 10–23. https://doi.org/10.1016/j.epsl.2017.02.005

Altunkaynak, S., & Dilek, Y. (2006). Timing and nature of postcollisional volcanism in western Anatolia and geodynamic implications. In Y. Dilek, & S. Pavlides (Eds.), *Postcollisional tectonics and magmatism in the Mediterranean region and Asia* (Vol. 409). Boulder, Colorado: Geological Society of America. https://doi.org/10.1130/2006.2409(17)

Andrews, E. R., & Billen, M. I. (2009). Rheologic controls on the dynamics of slab detachment. *Tectonophysics*, *464*(1-4), 60–69. https://doi.org/10.1016/j.tecto.2007.09.004

Arcay, D., Doin, M. P., Tric, E., Bousquet, R., & de Capitani, C. (2006). Overriding plate thinning in subduction zones: Localized convection induced by slab dehydration. *Geochemistry, Geophysics, Geosystems*, *7*, Q02007. https://doi.org/10.1029/2005gc001061

Arcay, D., Tric, E., & Doin, M. P. (2005). Numerical simulations of subduction zones—Effect of slab dehydration on the mantle wedge dynamics. *Physics of the Earth and Planetary Interiors*, *149*(1-2), 133–153. https://doi.org/10.1016/j.pepi.2004.08.020

Armijo, R., Lacassin, R., Coudurier-Curveur, A., & Carrizo, D. (2015). Coupled tectonic evolution of Andean orogeny and global climate. *Earth-Science Reviews*, *143*, 1–35. https://doi.org/10.1016/j.earscirev.2015.01.005

Arriagada, C., Cobbold, P. R., & Roperch, P. (2006). Salar de Atacama basin: A record of compressional tectonics in the central Andes since the mid-Cretaceous. *Tectonics*, *25*, TC1008. https://doi.org/10.1029/2004tc001770

Arriagada, C., Roperch, P., Mpodozis, C., & Cobbold, P. R. (2008). Paleogene building of the Bolivian orocline: Tectonic restoration of the central Andes in 2-D map view. *Tectonics*, *27*, TC6014. https://doi.org/10.1029/2008TC002269

Barnes, J. B., & Ehlers, T. A. (2009). End member models for Andean plateau uplift. *Earth-Science Reviews*, *97*(1-4), 105–132. https://doi.org/10.1016/j.earscirev.2009.08.003

Becker, T. W., Faccenna, C., O'Connell, R. J., & Giardini, D. (1999). The development of slabs in the upper mantle: Insights from numerical and laboratory experiments. *Journal of Geophysical Research*, *104*(B7), 15,207–15,226. https://doi.org/10.1029/1999jb900140

Billen, M. I. (2008). Modeling the dynamics of subducting slabs. *Annual Review of Earth and Planetary Sciences*, *36*, 325–356. https://doi.org/10.1146/annurev.earth.36.031207.124129

Billen, M. I. (2010). Slab dynamics in the transition zone. *Physics of the Earth and Planetary Interiors*, *183*(1-2), 296–308. https://doi.org/10.1016/j.pepi.2010.05.005

Butler, J. P., & Beaumont, C. (2017). Subduction zone decoupling/retreat modeling explains south Tibet (Xigaze) and other supra-subduction zone ophiolites and their UHP mineral phases. *Earth and Planetary Science Letters*, *463*, 101–117. https://doi.org/10.1016/j.epsl.2017.01.025

Butler, J. P., Beaumont, C., & Jamieson, R. A. (2015). Paradigm lost: Buoyancy thwarted by the strength of the Western Gneiss Region (ultra)high-pressure terrane, Norway. *Lithosphere*, *7*(4), 379–407. https://doi.org/10.1130/L426.1

Capitanio, F. A., Morra, G., & Goes, S. (2007). Dynamic models of downgoing plate-buoyancy driven subduction: Subduction motions and energy dissipation. *Earth and Planetary Science Letters*, *262*(1-2), 284–297. https://doi.org/10.1016/j.epsl.2007.07.039

Capitanio, F. A., Stegman, D. R., Moresi, L. N., & Sharples, W. (2010). Upper plate controls on deep subduction, trench migrations and deformations at convergent margins. *Tectonophysics*, *483*(1-2), 80–92. https://doi.org/10.1016/j.tecto.2009.08.020

Charrier, R., Pinto, L., & Rodríguez, M. P. (2007). Tectonostratigraphic evolution of the Andean orogen in Chile. In T. Moreno, & W. Gibbons (Eds.), *The geology of Chile* pp. 21–114). London: Geological Society of London. https://doi.org/10.1144/GOCH.3

Cizkova, H., van Hunen, J., van den Berg, A. P., & Vlaar, N. J. (2002). The influence of rheological weakening and yield stress on the interaction of slabs with the 670 km discontinuity. *Earth and Planetary Science Letters*, *199*(3-4), 447–457. https://doi.org/10.1016/S0012-821X(02)00586-1

Coira, B., Davidson, J., Mpodozis, C., & Ramos, V. (1982). Tectonic and magmatic evolution of the Andes of northern Argentina and Chile. *Earth-Science Reviews*, *18*(3-4), 303–332. https://doi.org/10.1016/0012-8252(82)90042-3

Conrad, C. P., & Hager, B. H. (1999). Effects of plate bending and fault strength at subduction zones on plate dynamics. *Journal of Geophysical Research*, *104*(B8), 17,551–17,571. https://doi.org/10.1029/1999jb900149

Currie, C. A., Beaumont, C., & Huismans, R. S. (2007). The fate of subducted sediments: A case for backarc intrusion and underplating. *Geology*, *35*(12), 1111–1114. https://doi.org/10.1130/G24098a.1

Currie, C. A., Ducea, M. N., DeCelles, P. G., & Beaumont, C. (2015). Geodynamic models of Cordilleran orogens: Gravitational instability of magmatic arc roots. *Geological Society of America Memoirs*, *212*, 1–22. https://doi.org/10.1130/2015.1212(01)

Currie, C. A., Huismans, R. S., & Beaumont, C. (2008). Thinning of continental backarc lithosphere by flow-induced gravitational instability. *Earth and Planetary Science Letters*, *269*(3-4), 435–446. https://doi.org/10.1016/j.epsl.2008.02.037

DeCelles, P. G., Ducea, M. N., Kapp, P., & Zandt, G. (2009). Cyclicity in Cordilleran orogenic systems. *Nature Geoscience*, *2*(4), 251–257. https://doi.org/10.1038/Ngeo469

Duretz, T., Schmalholz, S. M., & Gerya, T. V. (2012). Dynamics of slab detachment. *Geochemistry, Geophysics, Geosystems*, *13*, Q03020. https://doi.org/10.1029/2011gc004024

Erdos, Z., Huismans, R. S., van der Beek, P., & Thieulot, C. (2014). Extensional inheritance and surface processes as controlling factors of mountain belt structure. *Journal of Geophysical Research: Solid Earth*, *119*, 9042–9061. https://doi.org/10.1002/2014jb011408

Faccenda, M., Gerya, T. V., Mancktelow, N. S., & Moresi, L. (2012). Fluid flow during slab unbending and dehydration: Implications for intermediate-depth seismicity, slab weakening and deep water recycling. *Geochemistry, Geophysics, Geosystems*, *13*, Q01010. https://doi.org/10.1029/2011gc003860

Faccenna, C., Becker, T. W., Auer, L., Billi, A., Boschi, L., Brun, J. P., et al. (2014). Mantle dynamics in the Mediterranean. *Reviews of Geophysics*, *52*, 283–332. https://doi.org/10.1002/2013rg000444

Faccenna, C., Becker, T. W., Lallemand, S., Lagabrielle, Y., Funiciello, F., & Piromallo, C. (2010). Subduction-triggered magmatic pulses: A new class of plumes? *Earth and Planetary Science Letters*, *299*(1-2), 54–68. https://doi.org/10.1016/j.epsl.2010.08.012

Faccenna, C., Oncken, O., Holt, A. F., & Becker, T. W. (2017). Initiation of the Andean orogeny by lower mantle subduction. *Earth and Planetary Science Letters*, *463*, 189–201. https://doi.org/10.1016/j.epsl.2017.01.041

Forsyth, D., & Uyeda, S. (1975). Relative importance of driving forces of plate motion. *Geophysical Journal of the Royal Astronomical Society*, *43*(1), 163–200. https://doi.org/10.1111/j.1365-246X.1975.tb00631.x

Funiciello, F., Faccenna, C., & Giardini, D. (2004). Role of lateral mantle flow in the evolution of subduction systems: Insights from laboratory experiments. *Geophysical Journal International*, *157*(3), 1393–1406. https://doi.org/10.1111/j.1365-246X.2004.02313.x

Funiciello, F., Faccenna, C., Giardini, D., & Regenauer-Lieb, K. (2003). Dynamics of retreating slabs: 2. Insights from three-dimensional laboratory experiments. *Journal of Geophysical Research*, *108*(B4), 2207. https://doi.org/10.1029/2001jb000896

Garel, F., Goes, S., Davies, D. R., Davies, J. H., Kramer, S. C., & Wilson, C. R. (2014). Interaction of subducted slabs with the mantle transition-zone: A regime diagram from 2-D thermo-mechanical models with a mobile trench and an overriding plate. *Geochemistry, Geophysics, Geosystems*, *15*, 1739–1765. https://doi.org/10.1002/2014gc005257

Gerya, T. (2011). Future directions in subduction modeling. *Journal of Geodynamics*, *52*(5), 344–378. https://doi.org/10.1016/j.jog.2011.06.005

Gerya, T. V., Stern, R. J., Baes, M., Sobolev, S. V., & Whattam, S. A. (2015). Plate tectonics on the Earth triggered by plume-induced subduction initiation. *Nature*, *527*(7577), 221–225. https://doi.org/10.1038/nature15752

Gleason, G. C., & Tullis, J. (1995). A flow law for dislocation creep of quartz aggregates determined with the molten-salt cell. *Tectonophysics*, *247*(1-4), 1–23. https://doi.org/10.1016/0040-1951(95)00011-B

Goes, S., Agrusta, R., van Hunen, J., & Garel, F. (2017). Subduction-transition zone interaction: A review. *Geosphere*, *13*(3), 644–664. https://doi.org/10.1130/Ges01476.1

Gorczyk, W., Gerya, T. V., Connolly, J. A. D., & Yuen, D. A. (2007). Growth and mixing dynamics of mantle wedge plumes. *Geology*, *35*(7), 587–590. https://doi.org/10.1130/G23485a.1

Gorczyk, W., Willner, A. P., Gerya, T. V., Connolly, J. A. D., & Burg, J. P. (2007). Physical controls of magmatic productivity at Pacific-type convergent margins: Numerical modelling. *Physics of the Earth and Planetary Interiors*, *163*(1-4), 209–232. https://doi.org/10.1016/j.pepi.2007.05.010

Hacker, B. R. (1996). Eclogite formation and the rheology, buoyancy, seismicity, and $H_2O$ content of oceanic crust. In G. E Bebout, D. W. Scholl, S. H. Kirby, & J. P. Platt (Eds.), *Subduction: Top to bottom* (pp. 337–346). Washington, DC: American Geophysical Union. https://doi.org/10.1029/GM096p0337

Hacker, B. R., Kelemen, P. B., & Behn, M. D. (2011). Differentiation of the continental crust by relamination. *Earth and Planetary Science Letters*, *307*(3-4), 501–516. https://doi.org/10.1016/j.epsl.2011.05.024

Hacker, B. R., Kelemen, P. B., & Behn, M. D. (2015). Continental lower crust. *Annual Review of Earth and Planetary Sciences*, *43*(1h), 167–205. https://doi.org/10.1146/annurev-earth-050212-124117

Heuret, A., & Lallemand, S. (2005). Plate motions, slab dynamics and back-arc deformation. *Physics of the Earth and Planetary Interiors*, *149*(1-2), 31–51. https://doi.org/10.1016/j.pepi.2004.08.022

Holt, A. F., Becker, T. W., & Buffett, B. A. (2015). Trench migration and overriding plate stress in dynamic subduction models. *Geophysical Journal International*, *201*(1), 172–192. https://doi.org/10.1093/gji/ggv011

Horton, B. K. (2018). Tectonic regimes of the central and southern Andes: Responses to variations in plate coupling during subduction. *Tectonics*, *37*, 402–429. https://doi.org/10.1002/2017tc004624

Huang, Y., Chubakov, V., Mantovani, F., Rudnick, R. L., & McDonough, W. F. (2013). A reference Earth model for the heat-producing elements and associated geoneutrino flux. *Geochemistry, Geophysics, Geosystems*, *14*, 2003–2029. https://doi.org/10.1002/ggge.20129

Huangfu, P. P., Wang, Y. J., Cawood, P. A., Li, Z. H., Fan, W. M., & Gerya, T. V. (2016). Thermo-mechanical controls of flat subduction: Insights from numerical modeling. *Gondwana Research*, *40*, 170–183. https://doi.org/10.1016/j.gr.2016.08.012

Huismans, R. S., & Beaumont, C. (2003). Symmetric and asymmetric lithospheric extension: Relative effects of frictional-plastic and viscous strain softening. *Journal of Geophysical Research*, *108*(B10), 2496. https://doi.org/10.1029/2002jb002026

Huismans, R. S., & Beaumont, C. (2011). Depth-dependent extension, two-stage breakup and cratonic underplating at rifted margins. *Nature*, *473*(7345), 74–78. Retrieved from http://www.ncbi.nlm.nih.gov/pubmed/21544144 https://doi.org/10.1038/nature09988

Husson, L., Conrad, C. P., & Faccenna, C. (2012). Plate motions, Andean orogeny, and volcanism above the South Atlantic convection cell. *Earth and Planetary Science Letters*, *317*, 126–135. https://doi.org/10.1016/j.epsl.2011.11.040

Hyndman, R. D., Currie, C. A., & Mazzotti, S. P. (2005). Subduction zone backarcs, mobile belts, and orogenic heat. *GSA Today*, *15*(2), 4–10. https://doi.org/10.1130/1052-5173(2005)015<4:SZBMBA>2.0.CO;2

Jarrard, R. D. (1986). Relations among subduction parameters. *Reviews of Geophysics*, *24*(2), 217–284. https://doi.org/10.1029/RG024i002p00217

Jolivet, L., & Brun, J. P. (2010). Cenozoic geodynamic evolution of the Aegean. *International Journal of Earth Sciences*, *99*(1), 109–138. https://doi.org/10.1007/s00531-008-0366-4

Jolivet, L., Faccenna, C., Huet, B., Labrousse, L., Le Pourhiet, L., Lacombe, O., et al. (2013). Aegean tectonics: Strain localisation, slab tearing and trench retreat. *Tectonophysics*, *597*, 1–33. https://doi.org/10.1016/j.tecto.2012.06.011

Karato, S., & Wu, P. (1993). Rheology of the upper mantle—A synthesis. *Science*, *260*(5109), 771–778. https://doi.org/10.1126/science.260.5109.771

Katayama, I., & Karato, S. I. (2008). Low-temperature, high-stress deformation of olivine under water-saturated conditions. *Physics of the Earth and Planetary Interiors*, *168*(3-4), 125–133. https://doi.org/10.1016/j.pepi.2008.05.019

Kelly, S., Butler, J. P., & Beaumont, C. (2016). Continental collision with a sandwiched accreted terrane: Insights into Himalayan-Tibetan lithospheric mantle tectonics? *Earth and Planetary Science Letters*, *455*, 176–195. https://doi.org/10.1016/j.epsl.2016.08.039

Kreemer, C., Holt, W. E., & Haines, A. J. (2003). An integrated global model of present-day plate motions and plate boundary deformation. *Geophysical Journal International*, *154*(1), 8–34. https://doi.org/10.1046/j.1365-246X.2003.01917.x

Krystopowicz, N. J., & Currie, C. A (2013). Crustal eclogitization and lithosphere delamination in orogens. *Earth and Planetary Science Letters*, *361*, 195–207. https://doi.org/10.1016/j.epsl.2012.09.056

Lamb, S. (2011). Did shortening in thick crust cause rapid late Cenozoic uplift in the northern Bolivian Andes? *Journal of the Geological Society*, *168*(5), 1079–1092. https://doi.org/10.1144/0016-76492011-008

Li, Z. H., Liu, M. A., & Gerya, T. (2016). Lithosphere delamination in continental collisional orogens: A systematic numerical study. *Journal of Geophysical Research: Solid Earth*, *121*, 5186–5211. https://doi.org/10.1002/2016jb013106

Li, C., van der Hilst, R. D., Engdahl, E. R., & Burdick, S. (2008). A new global model for P wave speed variations in Earth's mantle. *Geochemistry, Geophysics, Geosystems*, *9*, Q05018. https://doi.org/10.1029/2007gc001806

Mackwell, S. J., Zimmerman, M. E., & Kohlstedt, D. L. (1998). High-temperature deformation of dry diabase with application to tectonics on Venus. *Journal of Geophysical Research*, *103*(B1), 975–984. https://doi.org/10.1029/97JB02671

Magni, V., Faccenna, C., van Hunen, J., & Funiciello, F. (2014). How collision triggers backarc extension: Insight into Mediterranean style of extension from 3-D numerical models. *Geology*, *42*(6), 511–514. https://doi.org/10.1130/G35446.1

Maloney, K. T., Clarke, G. L., Klepeis, K. A., & Quevedo, L. (2013). The late Jurassic to present evolution of the Andean margin: Drivers and the geological record. *Tectonics*, *32*, 1049–1065. https://doi.org/10.1002/tect.20067

Mitrovica, J. X., & Forte, A. M. (2004). A new inference of mantle viscosity based upon joint inversion of convection and glacial isostatic adjustment data. *Earth and Planetary Science Letters*, *225*(1-2), 177–189. https://doi.org/10.1016/j.epsl.2004.06.005

Moresi, L., Betts, P. G., Miller, M. S., & Cayley, R. A. (2014). Dynamics of continental accretion. *Nature*, *508*(7495), 245–248. https://doi.org/10.1038/nature13033

Morra, G., Regenauer-Lieb, K., & Giardini, D. (2006). Curvature of oceanic arcs. *Geology*, *34*(10), 877–880. https://doi.org/10.1130/G22462.1

Müller, R. D., Sdrolias, M., Gaina, C., & Roest, W. R. (2008). Age, spreading rates, and spreading asymmetry of the world's ocean crust. *Geochemistry, Geophysics, Geosystems*, *9*, Q04006. https://doi.org/10.1029/2007gc001743

O'Neill, C., Müller, D., & Steinberger, B. (2005). On the uncertainties in hot spot reconstructions and the significance of moving hot spot reference frames. *Geochemistry, Geophysics, Geosystems*, *6*, Q04003. https://doi.org/10.1029/2004gc000784

Oncken, O., Hindle, D., Kley, J., Elger, K., Victor, P., & Schemmann, K. (2006). Deformation of the central Andean upper plate system—Facts, fiction, and constraints for plateau models. In O. Oncken, et al. (Eds.), *The Andes Frontiers in Earth sciences* (pp. 3–27). Berlin, Heidelberg: Springer. https://doi.org/10.1007/978-3-540-48684-8n_1

Parsons, B., & Richter, F. M. (1980). A relation between the driving force and geoid anomaly associated with mid-ocean ridges. *Earth and Planetary Science Letters*, *51*(2), 445–450. https://doi.org/10.1016/0012-821x(80)90223-X

Pe-Piper, G., & Piper, D. J. W. (2006). Unique features of the cenozoic igneous rocks of Greece. In Y. Dilek, & S. Pavlides (Eds.), *Postcollisional tectonics and magmatism in the Mediterranean region and Asia* (vol. 409). Boulder, Colorado: Geological Society of America. https://doi.org/10.1130/2006.2409(14)

Pelletier, J. D., DeCelles, P. G., & Zandt, G. (2010). Relationships among climate, erosion, topography, and delamination in the Andes: A numerical modeling investigation. *Geology*, *38*(3), 259–262. https://doi.org/10.1130/g30755.1

Piromallo, C., & Morelli, A. (2003). P wave tomography of the mantle under the Alpine-Mediterranean area. *Journal of Geophysical Research*, *108*(B2), 2065. https://doi.org/10.1029/2002jb001757

Pope, D. C., & Willett, S. D. (1998). Thermal-mechanical model for crustal thickening in the central Andes driven by ablative subduction. *Geology*, *26*(6), 511–514. https://doi.org/10.1130/0091-7613(1998)026<0511:Tmmfct>2.3.Co;2

Pysklywec, R. N., & Beaumont, C. (2004). Intraplate tectonics: Feedback between radioactive thermal weakening and crustal deformation driven by mantle lithosphere instabilities. *Earth and Planetary Science Letters*, *221*(1-4), 275–292. https://doi.org/10.1016/S0012-821x(04)00098-6

Quinquis, M. E. T., Buiter, S. J. H., & Ellis, S. (2011). The role of boundary conditions in numerical models of subduction zone dynamics. *Tectonophysics*, *497*(1-4), 57–70. https://doi.org/10.1016/j.tecto.2010.11.001

Rapp, R. P., & Watson, E. B. (1995). Dehydration melting of metabasalt at 8–32 kbar—Implications for continental growth and crust-mantle recycling. *Journal of Petrology*, *36*(4), 891–931. https://doi.org/10.1093/petrology/36.4.891

Rodriguez-Gonzalez, J., & Negredo, A. M. (2012). The role of the overriding plate thermal state on slab dip variability and on the occurrence of flat subduction. *Geochemistry, Geophysics, Geosystems*, *13*, Q01002. https://doi.org/10.1029/2011gc003859

Schellart, W. P. (2008). Overriding plate shortening and extension above subduction zones: A parametric study to explain formation of the Andes mountains. *Geological Society of America Bulletin*, *120*(11-12), 1441–1454. https://doi.org/10.1130/B26360.1

Schellart, W. P., Freeman, J., Stegman, D. R., Moresi, L., & May, D. (2007). Evolution and diversity of subduction zones controlled by slab width. *Nature*, *446*(7133), 308–311. https://doi.org/10.1038/nature05615

Schellart, W. P., & Moresi, L. (2013). A new driving mechanism for backarc extension and backarc shortening through slab sinking induced toroidal and poloidal mantle flow: Results from dynamic subduction models with an overriding plate. *Journal of Geophysical Research: Solid Earth*, *118*, 3221–3248. https://doi.org/10.1002/jgrb.50173

Schellart, W. P., Stegman, D. R., & Freeman, J. (2008). Global trench migration velocities and slab migration induced upper mantle volume fluxes: Constraints to find an Earth reference frame based on minimizing viscous dissipation. *Earth-Science Reviews*, *88*(1-2), 118–144. https://doi.org/10.1016/j.earscirev.2008.01.005

Schmeling, H., Babeyko, A. Y., Enns, A., Faccenna, C., Funiciello, F., Gerya, T., et al. (2008). A benchmark comparison of spontaneous subduction models—Towards a free surface. *Physics of the Earth and Planetary Interiors*, *171*(1-4), 198–223. https://doi.org/10.1016/j.pepi.2008.06.028

Schurr, B., Rietbrock, A., Asch, G., Kind, R., & Oncken, O. (2006). Evidence for lithospheric detachment in the central Andes from local earthquake tomography. *Tectonophysics*, *415*(1-4), 203–223. https://doi.org/10.1016/j.tecto.2005.12.007

Seton, M., Müller, R. D., Zahirovic, S., Gaina, C., Torsvik, T. H., Shephard, G., et al. (2012). Global continental and ocean basin reconstructions since 200 Ma. *Earth-Science Reviews*, *113*(3-4), 212–270. https://doi.org/10.1016/j.earscirev.2012.03.002

Sobolev, S. V., & Babeyko, A. Y. (2005). What drives orogeny in the Andes? *Geology*, *33*(8), 617–620. https://doi.org/10.1130/G21557

Stevenson, D. J., & Turner, J. S. (1977). Angle of subduction. *Nature*, *270*(5635), 334–336. https://doi.org/10.1038/270334a0

Stüwe, K. (2007). *Geodynamics of the lithosphere* (2nd ed.). Berlin Heidelberg: Springer Verlag. https://doi.org/10.1007/978-3-540-71237-4

Thieulot, C. (2011). Fantom: Two- and three-dimensional numerical modelling of creeping flows for the solution of geological problems. *Physics of the Earth and Planetary Interiors*, *188*(1-2), 47–68. https://doi.org/10.1016/j.pepi.2011.06.011

Torsvik, T. H., Steinberger, B., Gurnis, M., & Gaina, C. (2010). Plate tectonics and net lithosphere rotation over the past 150 My. *Earth and Planetary Science Letters*, *291*(1-4), 106–112. https://doi.org/10.1016/j.epsl.2009.12.055

Tosi, N., Yuen, D. A., de Koker, N., & Wentzcovitch, R. M. (2013). Mantle dynamics with pressure- and temperature-dependent thermal expansivity and conductivity. *Physics of the Earth and Planetary Interiors*, *217*, 48–58. https://doi.org/10.1016/j.pepi.2013.02.004

Tsenn, M. C., & Carter, N. L. (1987). Upper limits of power law creep of rocks. *Tectonophysics*, *136*(1–2), 1–26.

Turcotte, D. L., & Schubert, G. (1982). *Geodynamics*. New York: John Wiley.

Uyeda, S., & Kanamori, H. (1979). Back-arc opening and the mode of subduction. *Journal of Geophysical Research*, *84*(Nb3), 1049–1061. https://doi.org/10.1029/JB084iB03p01049

Wessel, P., Harada, Y., & Kroenke, L. W. (2006). Toward a self-consistent, high-resolution absolute plate motion model for the Pacific. *Geochemistry, Geophysics, Geosystems*, *7*, Q03L12. https://doi.org/10.1029/2005GC001000

Wolf, M. B., & Wyllie, P. J. (1993). Garnet growth during amphibolite anatexis—Implications of a garnetiferous restite. *Journal of Geology*, *101*(3), 357–373. https://doi.org/10.1086/648229

Zhu, H. J., Bozdag, E., Peter, D., & Tromp, J. (2012). Structure of the european upper mantle revealed by adjoint tomography. *Nature Geoscience*, *5*(7), 493–498. https://doi.org/10.1038/ngeo1501